Marine Geology
October 2022, Volume 452, Pages 106900 (15p.)
https://doi.org/10.1016/j.margeo.2022.106900
https://archimer.ifremer.fr/doc/00792/90408/

Factors affecting thickness and frequency of turbidites triggered by earthquakes in Kumburgaz Basin, Sea of Marmara

Yakupoğlu Nurettin [1, *], Henry Pierre [2], Uçarkuş Gülsen [1], Eriş K. Kadir [1], Demory François [2], Crouzet Christian [3], Çağatay M. Namık [1]

[1] Istanbul Technical University, Geological Engineering Department, EMCOL Applied Research Center, Faculty of Mines, Ayazağa, 34469 İstanbul, Turkey
[2] Aix Marseille Univ, CNRS, IRD, INRAE, CEREGE, Aix-en-Provence, France
[3] ISTerre, Université Savoie Mont Blanc, Université Grenoble Alpes, CNRS, IRD, Université Gustave Eiffel, 73000 Chambéry, France

* Corresponding author : Nurettin Yakupoglu, email address : yakupoglu@itu.edu.tr

Abstract :

Submerged fault ruptures generate earthquake-triggered mass flow deposits, which are extensively used as a tool in subaqueous paleoseismology. In tectonically active deep sedimentary basins, such as the Sea of Marmara (SoM), these mass flow deposits are defined as turbidite-homogenite units (THUs), consisting essentially of a coarse basal part and an overlying homogeneous mud (homogenite). Detailed characterization of THUs is crucial in order to establish meaningful criteria to link these units with earthquakes events and to identify their transport routes and depositional mechanisms. Here, we combine μ-X-ray Fluorescence (μ-XRF), Anisotropy of Magnetic Susceptibility (AMS) and additional rock magnetism analyses of a 21-m long piston core from the Kumburgaz Basin of SoM to define the upper stratigraphic boundary of THUs with hemipelagic sediments and investigate the controls of hydrological changes on turbidite frequency and thickness over the last 15 kyrs BP. The sedimentary succession of this period includes a lower lacustrine and an upper marine unit with two Holocene sapropel intervals. The sequence is interrupted by a total of 70 THUs, characterized by a significant magnetic foliation related to the depositional setting rather than the magnetic signature. Magnetic mineralogy of the coarse basal parts of THUs have more ferromagnetic particles than the overlying homogenites and background sediments. While the homogenite parts have a more constant mineralogy than the basal parts, they do not differ the background sediments.

Based on an event-free chronostratigraphic model derived from radiocarbon ages and the published age of lacustrine-marine (L-M) transition, the average THU occurrence intervals in the lacustrine (14.8–12.6 kyrs BP), lower sapropel (11.2–5.7 kyrs BP), upper sapropel (5.4–2.7 kyrs BP) and non-sapropelic part of the marine unit (2.7 kyrs BP-present) are 235 yrs., 287 yrs., 114 yrs. and 160 yrs. respectively. The average thickness of the THUs in the same units are 20.8 cm, 15.7 cm, 6.1 cm and 6.1 cm. The variability of average THU occurrence intervals and THU thicknesses are controlled by the sea level rise and salinity increase following the full marine connection of the SoM at 12.6 kyrs BP, which caused changes in slope stability, sediment composition and sediment deposition in different parts of the basin. Geomechanical

properties of the lower sapropel appears to have been important in resulting long THU recurrence intervals and relatively high THU thicknesses.

Highlights

► Multi-proxy parameters (XRF, AMS) are used to demarcation turbidite-homogenite units in the Kumburgaz Basin. ► 15 kyrs long sedimentary record of turbidite-homogenite units containing marine and lacustrine phases of Sea of Marmara. ► Turbidite-Homogenite intervals and thicknesses are affected by climatic changes, sea level and salinity of the region.

Keywords : Subaqueous paleoseismology, Turbidite-Homogenite, Sea of Marmara, Kumburgaz Basin, Anisotropy of Magnetic Susceptibility

1. Introduction

Many years after rock magnetic studies led on marine sediments (Harrison & Funnell, 1964; Opdyke et al., 1966), similar approaches were done in subaqueous environments dealing with a broad spectrum of problems related to (a) instantaneous sedimentary processes (Hiscott et al., 1997; Ge et al., 2012; Campos et al., 2013; Stachowska et al., 2020), (b) major past-climatic events (Kruiver et al., 1999; Demory et al., 2005a; Drab et al., 2015a), and (c) environmental changes (and resilience of sedimentary environments) (Pozza et al., 2004; Franke et al., 2009; Akinyemi et al., 2013; Nizou et al., 2016). Instantaneous sedimentary processes include subaqueous landslides and mass-flows that result in deposition of debris flows, mudflows and turbidites. They can be triggered by earthquakes (Shiki et al., 2000; Nakajima and Kanai, 2000; Goldfinger et al., 2003, 2017; Beck et al., 2007), storm waves (Prior et al., 1989), hyperpycnal flows (Mulder and Syvitski, 1995), gas hydrate dissociations (Bourry et al., 2009), sediment overloading (Nemec, 1990; Chapron et al., 1999), volcanic eruptions (Cita and Aloisi, 2000) and floods (Beck et al, 1996). In tectonically active sedimentary basins, turbidite units are common and occur interbedded with hemipelagic or pelagic sedimentary sequences. The most common triggering mechanism of turbidites in such basins is the seismic activity of submerged fault systems (Goldfinger et al., 2011; Çağatay et al., 2012; McHugh et al., 2014; Avşar et al., 2015; Yakupoğlu et al., 2019; Gastineau et al., 2021). Hence, turbidites have been widely used as a tool in subaqueous paleoseismology in different settings, including in the Sea of Marmara (SoM) (Adams, 1990; Nakajima and Kanai, 2000; Shiki et al., 2000; Gorsline et al., 2000; Goldfinger et al., 2003, 2007, 2008, 2017; Sarı and Çağatay, 2006; Beck et al., 2007; Goldfinger, 2011; Çağatay et al., 2012; Drab et al., 2012, 2015; Eriş et al., 2012; Pouderoux et al., 2012a, 2012b; Gutiérrez-Pastor et al., 2013; Barnes et al., 2013; Polonia et al., 2013, 2017; McHugh et al., 2014; Moernaut et al.,

2014, 2017; Patton et al., 2015; Avşar et al., 2015; Van Daele et al., 2017; Yakupoğlu et al., 2019; Ikehara et al., 2020; Wils et al., 2020; Gastineau et al., 2021).

Seismically triggered turbidites commonly consist of a coarse basal part (T: Turbidite Body) and an overlying homogenous silt-clay size cap (H: Homogenite, muddy turbidite or turbidite tail), and commonly termed as turbidite-homogenite units (THU). The term homogenite broadly represents the "Bouma E" sublayer that contains homogenous mud deposited from the suspension cloud of a turbidity current. Thick (>1 m) homogenite layers can be imaged as seismically transparent facies in high-resolution seismic reflection profiles (Kastens and Cita, 1981; Cita and Rimoldi, 1997; Beck et al., 2007; McHugh et al., 2011; Eriş et al., 2012). However, homogenites are hardly distinguished from the overlying hemipelagic sediments using the usual physical and sedimentological properties such as gamma density and grainsize parameters (Çağatay et al., 2012; Eriş et al., 2012; Barnes et al., 2013; McHugh et al., 2014; Goldfinger et al., 2017; Yakupoğlu et al., 2019). These deposits have been recently best distinguished from the background hemipelagic sediments using the magnetic foliation determined from Anisotropy of Magnetic Susceptibility (AMS) measurements (Ge et al., 2012; Campos et al., 2013; Petersen et al., 2014; Tamaki et al., 2015; Rapuc et al., 2018; Stachowska et al., 2020). A clear demarcation of these boundaries is important for construction of a robust age-depth model based on an event-free stratigraphy, which can then be used dating THUs and establishing long-term paleoseismological records (Beck et al., 2009; Goldfinger, 2011; Barnes et al., 2013; Yakupoğlu et al., 2019),

The SoM, being located along the North Anatolian Fault (NAF), is an important location for subaqueous paleoseismological studies (e.g. Çağatay et al., 2012; Eriş et al., 2012; Drab et al., 2012; McHugh et al., 2014; Drab et al., 2015b; Yakupoğlu et al., 2019). Moreover, because of its interesting oceanographic setting between the Aegean (Mediterranean) Sea and Black Sea, its environment alternated between lacustrine and marine,

with latest marine connection taking place ~12.6 cal yrs BP and ensued sapropel formations during c.12.3 - 5.7 cal kyrs and 5.4 and 2.7 cal kyrs BP (Çağatay et al., 2015).

In this study, we integrate micro-X-Ray Fluorescence (μ-XRF) elemental geochemistry, AMS and other rock magnetism analyses of a Calypso core (MRS CS-14) from the Kumburgaz Basin of SoM with two main objectives: (1) to distinguish the boundary between the homogenite layers of the THUs and overlying background hemipelagic sediments, and (2) to understand how sea level and salinity rise control turbidite thickness and frequency during different phases of the lacustrine and marine periods in the last 15 kyrs, based on a robust, event-free age-depth model. Our findings from this integrated approach contribute to the understanding of hydrological and seismotectonic controls on turbidite generation in a tectonically active restricted basin, where tsunami generation (including reflection and seiche effect) would be also expected (e.g. Beck et al., 2007; Çağatay et al., 2012: Ashi et al., 2014).

2. Tectonic and oceanographic setting

SoM is located in the NW part of Turkey and the western termination of the 1600-km long NAF Zone. The deformation zone includes three main branches where northern and middle branches of NAF are submerged faults systems within the SoM (Fig. 1). Based on GPS rates, 75 percent of the plate motion is transferred on the northern branch of NAF (NNAF) (~18-20 mm/yr) with the remainder being accommodated on the southern branches (Reilinger et al., 1997; Straub et al., 1997; McClusky et al., 2000; Le Pichon et al., 2001; Armijo et al., 2002; Provost et al., 2003; Flerit et al., 2003; Şengör et al., 2005; Reilinger et al., 2006). NNAF passes through three fault-controlled basins, which from west to east are Tekirdağ (−1133 m), Central (−1268 m), and Çınarcık (−1276 m) basins, that are separated by the Western and Central highs (Fig. 1).

The SoM is connected to the Black Sea and Aegean Sea via the Bosphorus and Dardanelles straits, respectively (Fig. 1). This connection allows exchange of two water masses of different salinities; Mediterranean water (~38.5 psu) and Black Sea water (~18 psu) results in a two-way water current system with a permanent pycnocline at -25 m in the SoM (Ünlüata et al., 1990; Beşiktepe et al., 1994; Chiggiato et al., 2012; Aydoğdu et al., 2018). Renewal time of the upper and lower water masses of the SoM is 5-6 months and 6-7 years, respectively (Beşiktepe et al., 1994). The fluvial water and sediment input to the SoM is mainly from its southern catchment region by Kocasu, Gönen and Biga rivers ($2.2x10^6$ t/yr suspended material) (EIE, 1993; Kazancı et al., 2004).

During the Late Quaternary glacial-interglacial cycles, the environmental conditions in SoM alternated between lacustrine and marine, being controlled by the sills depths in the Dardanelles and Bosphorus, currently at -65 mbsl and -35 mbsl, respectively (e.g. Çağatay et al., 2000, 2015, 2019; Eriş et al., 2007). The last reconnection of the SoM with the Aegean Sea is dated between 14.7 kyr (initial connection, Vidal et al., 2010) and 12.6 kyr BP (full connection, Çağatay et al., 2015) and with the Black sea at c. 9 kyr BP (Major et al., 2006; Ryan, 2007). After the last marine reconnection, two sapropels were deposited in the SoM: Lower Sapropel (12.3-5.7 kyr BP, Çağatay et al., 1999, 2003, 2015; Vidal et al., 2010) and the Upper Sapropel (5.4-2.7 kyr BP, Çağatay et al., 1999; Tolun et al., 2002).

Kumburgaz Basin, where the studied core is located, is a depression located on the Central High with maximum depth of 880 m. It is a 35 km long, 11 km wide, ENE-trending depression, covering an area of 160 km^2 and bounded by NNAF to its north (Fig. 1; Çağatay and Uçarkuş, 2019). Continental slope to the north is marked by two amphitheater-like canyons. The eastern canyon is located off Büyük Çekmece Lagoon. The rocks exposed in the catchment area of the Kumburgaz Basin include Paleozoic schists and meta-granites and the overlying Eocene reefal limestones and Oligocene-Miocene sandstones and mudstones

(Alp, 2014; Dalgıç, 2004). The basin has a sedimentation rate (2 to 2.5mm/yr) for Holocene period but two to three times higher rates for the lacustrine late glacial period (~5.4 mm/yr) (Beck et al., 2007).

3. Material and methods

3.1 Cores and multi-parameter analyses

Two ~21-m-long calypso cores CS-01 (28.50362/40.87140; 834 mbsl) (Yakupoğlu et al., 2019 and see figures therein) and CS-14 (28.47740/40.85360; 820 mbsl) were recovered from Kumburgaz Basin during the 2014 EC FP7 MARsite project cruise by *RV "Pourquoi pas?"* (Figs. 1B, 2). The core CS-14 was split into 1 m long sections (21 sections), and core sections were split into two halves. One half was photographed, visually logged sampled for rock magnetism analyses Istanbul Technical University (ITU) Eastern Mediterranean Centre for Oceanography and Limnology (EMCOL). Core sections were split into two halves. Another half is used for Non-destructive analyses at the ITU-EMCOL core analysis laboratory, using Itrax μ-XRF core scanner and Geotek Multi Sensor Core Logger (MSCL). The core scanner was used for elemental composition (Fe, K, Ca, Sr, Mn) and digital X-ray radiography, and operated at 1 mm resolution and 20 s measurement time, using a Mo X-ray tube powered at of 30 kV and 50 mA. The MSCL was used for gamma density (GD) measurements at 10 mm resolution (Figs. 4-6). Total Organic Carbon (TOC) (difference between total carbon and total inorganic carbon (TIC)) analyses were performed using a Shimadzu TOC/TIC analyzer at ITU-EMCOL. Before the analysis, samples were dried in a freeze-dryer and processed on an augite mortar. Thus, total carbon content was measured by burning the sample at 900°C in a catalytic combustion furnace. For total inorganic carbon content, samples were treated with 85% phosphoric acid under 200°C, and the evolved carbon dioxide was measured by the detector. TOC concentration is calculated as the difference

between total carbon and total inorganic carbon content. The precision for TOC and TIC analyses were 2% at 95% confidence level. (Fig. 3).

3.2 Anisotropy of magnetic susceptibility and rock magnetism analyses

All magnetic measurements were conducted in the Rock Magnetic Laboratory of the CEREGE (Aix-Marseille University). A total of 879 samples were collected using 8 cm^3 plastic boxes directly pushed into the sediment. For those samples, AMS was measured using AGICO MFK1-FA Kappabridge. The magnetic susceptibility tensors deduced from AMS measurements are characterized by three principal components (χ_{max}, χ_{int} and χ_{min}) and angles (declination and inclination) defining their orientation in the split-core reference frame (Jelinek, 1981; Hrouda, 1982; Tarling & Hrouda, 1993). Additionally, magnetic lineation (χ_{max}/χ_{int}), magnetic foliation (χ_{int}/χ_{min}) and mean tensorial magnetic susceptibility ($\chi_m=(\chi_{max}+\chi_{int}+\chi_{min})/3$) were calculated for each specimen.

In order to characterize magnetic mineralogy, two types of laboratory remanent magnetizations were artificially imparted on 98 samples through the core: Anhysteretic Remanent Magnetization (ARM) and Isothermal Remanent Magnetization (IRM). ARM was produced in-line and measured with the SRM760R using a 100 mT alternating field with a bias field of 50 µT. The ARM was also measured after a demagnetization step of 30 mT (ARM_{30}). The ratio ARM_{30}/ARM deduced from ARM measurements is a magnetic grain size indicator valid for constant low-coercive magnetic fraction (Johnson et al., 1975; Rochette et al., 1992; Tarling & Hrouda, 1993; Stoner & St Onge, 2007; Campos et al., 2013; Nizou et al., 2016). Isothermal Remanent Magnetization (IRM) was acquired at 3 T, measured and then at 0.3 T in the opposite direction using a pulse magnetizer MMPM9 from Magnetic Measurements Ltd. From these measurements, S-ratio was calculated by using formula (1-IRM-$_{0.3T}$ / $SIRM_{3T}$)/2. S-ratio is a parameter of the relative abundance of high coercivity

minerals with values close to 1 for magnetite and decreasing with increased proportion of high coercivity minerals (Bloemendal et al., 1992; Demory et al., 2005b).

3.3 Chronology and age-depth model

Accelerator Mass Spectrometry ^{14}C analyses of four samples were carried out at the TÜBİTAK-MAM (İzmit-Turkey) Radiocarbon Laboratory. Hemipelagic sediment samples from beneath the mass-flow units were wet-sieved, and >63 μm fractions were used to hand-pick carbonate shell material under binocular microscope. Dated materials were epifaunal benthic foraminifera, echinoderm spicules and occasionally bivalve shells, in addition to the planktonic foraminifera. Care was taken to sample whole shells without evidence of reworking and diagenesis. All samples were washed in distilled water and dried (at 40 °C) before the analysis. Results were calibrated using Calib v7.0 software with Marine13 ^{14}C calibration curve (Reimer et al., 2013) and a reservoir age correction of 390 ± 85 for marine (Siani et al., 2000) and 900 ± 100 for lacustrine samples (Çağatay et al., 2015) (Table 1). Inclusion of benthic and pelagic shells in the same sample would not affect the reservoir age because of the negligible difference (6–7 years) between the residence time of upper and lower water masses in the SoM (Beşiktepe et al., 1994). In addition to the calibrated ages, we used the previously dated lacustrine-marine (L-M) transition as dating point for the age-depth modelling (Table 1). The two sapropel layers in the core were defined in 2.3-5.9 mbsf and 6.3-15.4 mbsf intervals, using mainly by TOC analysis, as well as lithological and physical properties (Fig. 4), and were previously dated by several authors in the SoM (Çağatay et al., 1999, 2003, 2015; 2019; Tolun et al., 2002; Vidal et al., 2010; Filikçi et al., 2017). L-M transition in the SoM was previously dated to be between 14.7 cal kyrs BP (for the initial connection) and 12.6 cal kyrs BP (full connection) (Çağatay et al., 2015; Vidal et al., 2010). The L-M transition is marked by a 30 cm-thick coarse shelly sand layer between 17.18-17.48

mbsf in core CS-14, which is characterized by high χ_m (450 10^{-6} SI) values and a positive Mn excursion (>800 cps) (Fig. 3; Section 4.1).

For the age-depth modelling of core CS-14, all THUs thicknesses were discarded to obtain an event-free composite depth, and all calibrated ages were processed with R-studio using the script "CLAM" non-Bayesian method (Blaauw, 2010). The script created age-depth model, calculating the 95% Gaussian confidence interval around the best model (Fig. 4).

4. Results

4.1 Core lithology and geochemistry

The 21 m-thick sedimentary sequence in core CS-14 consists of a lower lacustrine unit and an upper marine unit on the bases of lithology, color, physical properties and fossil content (Figs. 2-4; Table 1). The boundary between the two units is located at c. 17.18 mbsf and the entire core sequence includes 70 THUs.

The marine unit is characterized by grey-green clayey-silty mud containing marine euryhaline molluscs, and benthic and planktonic foraminifera (Fig. 3). The uppermost ~2.3 mbsf of the marine unit contains homogenous fine silty clay showing a gradual downward change in color from brownish (oxidized mud) to light olive gray mud intercalated with twelve thin (average of 0.1 cm) THUs (Fig. 3; Table 2). The background sediments in this topmost unit are deposited at a rate of 0.79 m/kyr, and characterized by high χ_m values (~200 10^{-6} S.I) and low TOC (<1%) (Fig. 4; Table 2). The marine interval between 2.3-5.9 meters contains an olive gray homogenous silty clay with an oily luster, having ~1-1.5 % TOC and relatively low χ_m (~20 10^{-6} S.I) values (Fig. 4; Table 2). According to its TOC content, the interval between 2.3-5.9 mbsf corresponds to the upper sapropel in the SoM (Çağatay et al., 1999, 2015; Tolun et al., 2002). This sapropel contains 21 silty TH units within the range of 2.4-14.5 cm (Figs. 3-5; Table 2). Event-free part of the sapropel is deposited 0.68 m/kyr.

Below the upper sapropel, the marine unit between 5.9-6.3 mbsf is green grey mud intercalated with two THUs with average of 5.1 cm in thickness thus, having 1.2-1.8% TOC concentration and sedimentation rate of 0.95 m/kyr (Fig. 4; Table 2).

The underlying interval between 6.3-15.4 mbsf is relatively dark green grey, laminated mud with an oily luster. It contains abundant Fe-monosulphide nodules and patches and high TOC contents of up to 3 % (Figs. 3,4; Table 2). Considering its lithological properties, the 6.3-15.4 mbsf interval is correlated with the lower sapropel which was previously identified in the SoM by different workers (e.g., Çağatay et al., 2000; Tolun et al., 2002; Vidal et al., 2010). The event-free sapropel unit was deposited at a rate of 1.12 m/kyr (Fig. 4;). This interval contains 21 THUs in range of 3.5 to 59 cm (Table 2).

The marine interval between 15.4-17.2 mbsf a homogenous green gray clayey-silty marine mud with scarce Fe-sulfide nodules and benthic foraminifera and without oily luster and laminations (Figs. 3,4). This unit contains up to 2.5 % TOC in the lower part, which is mainly of terrestrial origin according to C/N and C-isotope analysis (Tolun et al., 2002). Event-free (background part) of the unit is deposited at a rate of 0.96 m/kyr. In this interval, four THUs composed of silty clayey fractions are observed with average of 11.1 cm in thickness. (Table 2). The underlying interval between 17.18 - 17.48 mbsf is a brownish grey, coarse sand layer that separates the overlying marine sequence from the underlying lacustrine sequence (i.e. L-M transition) (Figs. 3). It contains large marine and lacustrine bivalve shell fragments, abundant black Fe-monosulfides spots, mm-size pyrite concretions and secondary gypsum crystals, and is characterized by a high (c. 700 cps) Mn pulse and up to c. 500 10^{-6} SI χ_m values (Figs. 3-5). The lacustrine unit below 17.48 mbsf in the core consists of brownish light gray clayey-silty, massive mud, including fresh-brackish bivalves (*Dreissena* sp.) intercalated with 10 THUs. The unit have up to 51 cm thick THUs (average of 20.8 cm), with its event-free background sediments deposited at a rate of 0.8 m/kyr (Figs. 3,4; Table 2).

4.2 Sedimentology and geochemistry of turbidite-homogenite units

A total of 70 THUs consisting of a basal coarse part and an overlying turbiditic mud (homogenite) were identified based on lithological, physical and geochemical properties (Figs. 3-6). The lower boundaries of the coarse basal part of the turbidites with the underlying hemipelagic sediments are commonly sharp showing no scour and fill structures indicating non-erosional base (Fig. 6) except some sandy thicker THUs in lower sapropel and lacustrine phase (Fig. 6). The abrupt lithological change between the lower coarse basal parts and the upper homogeneous parts is detected in GD (gamma density), χ_m, Ca, Sr, Fe profiles and digital X-ray radiography images (Figs, 3, 6). Starting from middle of the lower sapropel frequent, positive Mn excursions occurs in the top 11 m part of the sequence and at the L-M transition (Figs. 4, 6). The upper boundary of homogenites of most THUs with the overlying background sediments are not clearly discernable visually and in the µ-XRF elemental profiles while some THUs show decrease in Fe and Ca at the boundary (Fig. 6). In contrast, homogenite lower boundaries are commonly marked by a sharp change from parallel, silty laminae of the coarse basal parts to massive mud of the homogenites. Some THUs' basal parts in the core sequence are stacked without the homogenite part or hemipelagic sediments in between (Fig. 3). The homogenites consist mainly of massive, fine silty clay, and have lower GD values than the coarse basal parts but slightly higher GD values than the hemipelagic sediments (Figs. 3, 6). However, transition from the homogenites into the overlying background sediments are not clearly visible in the digital radiographic images (Figs. 3,6). Details about the thicknesses of the THUs and their coarse basal and homogenite parts in the different chronostratigraphic units are described in Section 4.4.

4.3 Magnetic properties of turbidite-homogenite units

In order to better characterize the boundaries between the THUs and overlying background hemipelagic sediments, and the magnetic signature of the different chronostratigraphic units, we derived magnetic foliation, lineation and mean susceptibility precursors from the AMS (Figs. 5, 6). First 10 mbsf show magnetic foliation values of ~1.03-1.04, interrupted by positive spikes of the THUs (Fig, 5). The sequence between 10 to 17 mbsf contains high background foliation values (up to 1.06), regardless of the THU positive spikes, compared to the lacustrine background sediments (17.4-21 mbsl; foliation: 1.02-1.03). (Fig. 5). We observe a stable background foliation trend throughout the core, which reveals the magnetic characteristics of the THUs with positive excursions. Regardless of the TH lithology, AMS displays positive anomalies both on the coarse basal and homogenite parts of the sequence, with similar foliation values of 1.04-1.10 and 1.04-1.06, respectively (Figs, 5, 6). The boundary between homogenite and overlying background sediment shows a sharp drop on magnetic foliation on most of the THUs (Figs. 3, 6). Magnetic lineation has very low values throughout the core (1-1.03) (Figs. 5,6). Only some THUs have relatively high lineation (>1.007) having a positive pulse in coarse basal parts (Figs. 3, 5, 6).

Analysis of 98 samples from the core provided S-ratio, SIRM, ARM_{30}/ARM ratios in order to determine the magnetic characteristics of the lithological facies (Fig. 5). Accordingly, three lithologically different sections are identified corresponding to the coarse basal parts (18 samples), homogenites (7 samples) and background sediments (13 samples). S-ratio of these samples provided a scarce distribution (0.93-0.99). First 7 m of the core have the lowest values (0.93-0.96) (Fig. 5). Rest of the core have high S-ratios (0.96-0.99). ARM_{30}/ARM profile shows a narrow distribution in the core (0.2-0.6; have 0.43 average) (Fig. 5). In 9-14 mbsf interval, ARM_{30}/ARM has the lowest values (down to 0.2). The SIRM is rather constant along the core with values of 1-2 mA m^{-1} (Fig. 5). Still, several positive increments are observed in first 2 m and 18-21 m interval (Fig. 5).

Three selected THUs (THUs, A, B, C) were studied in detail to display the magnetic characteristics of THUs and background sediments in the main lithological units (i.e. marine, sapropel and lacustrine) (Figs. 3, 5, 6). In THU-A, ARM_{30}/ARM values oscillate between 0.40-0.45 and S-ratio is between 0.95-0.98. Foliation, lineation and χ_m of the coarse basal part show positive pulses (up to 1.06, 1.01 and up to 2.5k 10^{-6} SI, respectively). Homogenite part of THU-A is characterized by a decreasing foliation trend (down to 1.02) (Fig. 6).

THU-B is an amalgamated turbidite containing an Fe-depleted coarse base, which is overlain by a Ca-rich coarse sediment. In this interval, S-ratio has a decreasing trend (down to 0.96), whereas ARM_{30}/ARM shows increasing trend with values up to 0.3 (Fig. 6). In the homogenite part of THU-B, the ratio shows an increasing trend from 40% to %80. Foliation profile has a positive pulse at the top of the coarse basal part and a high stable value over the homogenite (1.03-1.05), whereas lineation only has a positive pulse at the coarse basal part of the unit (up to 1.01). In THU-B, χ_m have higher values than the overlying background sediments (up to 60-80 10^{-6} SI) (Fig. 6).

In both coarse basal and homogenite parts of THU-C, ARM_{30}/ARM values range between 0.35-0.65 and S-ratio shows a fluctuating trend between 0.97 and 0.99 (Fig. 6). Foliation and lineation profiles give positive pulses in the coarse basal part of this THU, with up to 1.1 and 1.03, respectively. In the homogenite part, foliation values range between 1.04 and 1.05), which are higher than those in the overlying background sediments (1.03-1.04) (Fig. 6). χ_m profile has a peak in the coarse basal part of THU-C (up to 250 10^{-6} SI) but low values in the homogenite part (~50 10^{-6} SI) (Fig. 6).

4.4 Average occurrence interval and thickness variation of turbidite-homogenite units in different chronostratigraphic units

The age-depth model of core CS-14, based on four Accelerated Mass Spectrometry ^{14}C ages and one chronostratigraphic horizon (i.e. L-M transition) (Table 2), is presented in Fig. 4. "Clam" cubic spline script of this model allows us to determine the individual ages of 70 THUs in the core and their average occurrence interval (or event frequency) in the different chronostratigraphic units, including the lacustrine and marine units and the two sapropel layers (Table 2, Supplementary Table). According to the model, the sedimentary sequence of core CS-14 extends back to c.15 cal kyrs BP and hence, the lacustrine unit was deposited between 14.8 and 12.6 cal kyrs BP (Fig. 4). The model also provides ages for the lower and upper sapropels within intervals of 11.2-5.7 kyrs BP and 5.4-2.7 kyrs BP, respectively (Fig. 4).

Using the age model, we determined the average occurrence interval of the THUs in different chronostratigraphic units of the core CS-14, which were defined based on visual observations, µ-XRF elemental and AMS profiles (Table 2; Supplementary Table). The lacustrine unit deposited during a ~2.4 kyr interval in the core includes 10 THUs, with an average occurrence interval of 235 yrs (Figs. 3, 4; Table 2; Supplementary Table). During the 5.5 kyr long lower sapropel interval, 21 THUs were deposited with an average occurrence interval of 287 yrs. The Upper sapropel with a depositional period of 2.7 kyrs has 21 THUs deposited with 114 yrs of average THU occurrence interval. The recent marine interval above the upper sapropel contains 12 THUs with an average occurrence interval of 160 yrs (Table 2). The average THU thicknesses and their percentages in the same units, from bottom to top, are 20.8, 15.7, 6.2 and 6.1 cm, and 30, 38, 35, and 53 %, respectively. The coarse basal part-to-homogenite part (TB-TT) thickness ratio range from an average of 0.3 (range: 0.1-0.5, neglecting on outlier value of 0.9) in the lacustrine unit to 0.9 (0.5-1.2) in the non-sapropelic marine unit below the lower sapropel (Supplementary Table 1). A gradual increase is observed in the average TB-TT thickness ratio from the lower sapropel (average. 0.6; range:

0.3-1.2) through upper sapropel (0.7; 0.2-1.1) to the upper non-sapropelic marine unit (0.8; 0.3-2).

5. Discussion

5.1 Factors controlling the magnetic properties of lacustrine and marine units and sapropels

Chronostratigraphic units of core CS-14 sequence show significant variations in all magnetic parameters. The core spans to the last ~15 kyrs BP with the earliest ~2.4 kyrs representing the lacustrine unit (Figs. 3,4). It has higher SIRM values than marine and sapropelic sediments, which are possibly related to higher content in ferromagnetic minerals inferred by higher mean susceptibility and relatively higher foliation (Fig. 5). The shelly sand layer with positive magnetic susceptibility and foliation pulses marking the L-M transition is interpreted to be a debrite (Figs. 3-5). Such unusual layers at the transition were previously reported in sediment cores from elsewhere in the SoM, and interpreted to be due to carbonate shell accumulation, inorganic carbonate precipitation and microbial reactions induced by mixing of lacustrine and marine waters (Çağatay et al., 2009, 2015, 2019; Eriş et al., 2011, 2019; Filikçi et al., 2017).

Despite the presence of the two sapropelic layers, the marine facies are characterized by relatively low χ_m (<50 x10^{-6} SI) similar to the cores from the Çınarcık, Tekirdağ and Central basins (Beck et al 2007; Drab et al., 2012; 2015a). The exception to this is the high χ_m values (>120 x10^{-6} SI) for the upper 2.2 m of the core, which represents the active diagenetic (redox) zone including the oxidized layers (Figs. 4, 5). This oxidized layer is accompanied also with low S-ratio and high SIRM, suggesting hematite enrichment.

Lower sapropelic sediments have significantly lower ARM_{30}/ARM in comparison to the rest of the marine sediments, indicating larger magnetite grain size. Indeed, the high S-

ratio and low ARM_{30}/ARM suggest accumulation of magnetite (Fig. 5). The upper sapropelic layer possess low TOC values (1 – 1.5%) compared to the lower sapropel (Fig. 4). This layer is characterized by low χ_m despite the increment of hematite contribution to the magnetic signal (lower S-ratio and higher SIRM) (Fig. 5). Relatively low TOC enrichment in the upper sapropelic layer explains the low degree of sulfurization of the iron oxides including hematite. Background foliation profile has low values in the lower sapropel supported by relatively low χ_m (Fig. 5). Even though S-ratio indicates that upper sapropel layer contains a portion of hematite, this could indicate that the magnetic signature is carried by both magnetite and hematite in this interval (Fig. 5) (Drab et al., 2015a).

5.2. Sedimentological, geochemical and magnetic properties of turbidite-homogenite units: Demarcation between homogenite and background hemipelagic sediments

Sedimentological, geochemical and physical (gamma density and lithology) properties of the THUs in Kumburgaz Basin core CS-14 are quite similar with those documented from the other basins in the SoM (McHugh et al., 2006, 2014; Beck et al., 2007; Çağatay et al., 2012; Eriş et al., 2012; Drab et al., 2015b; Yakupoğlu et al., 2019). Overall background sediments display more variability depending on facies than THU sediments.

The coarse basal part of THUs (Fig. 6A) in the marine unit is represented by parallel lamination and a sharp basal contact with the underlying background sediments. The basal parts have a higher magnetic susceptibility and higher content in ferromagnetic grains. In the marine THU example (Fig. 6A), coarse basal part has stronger foliation and lineation than both the homogenites and background sediment. All THU units in the non-sapropelic facies except some thinner examples have higher foliation than the overlying background sediments (Figs. 3, 6). However, the transition upward is often progressive, and may be difficult to pinpoint based on AMS data alone. This is especially true for the thinner events as the

maximum resolution of AMS data is 2 cm. Therefore, we have also taken into account the radiographic images (pattern changes light to dark) and geochemical elemental distribution of THUs (especially trends of Fe, Ca and Sr) to define the upper boundaries more precisely. The positive magnetic foliation anomaly is not entirely correlated to the variations of other magnetic properties (see Fig. 6; ARM_{30}/ARM and S-ratio profiles). In average, the turbidite layers appear to have a slight (but statistically significant) increase of ARM_{30}/ARM compared with both homogenites and background sediments.. The distinction of homogenite-coarse basal unit is rather visible in the core photographs and radiography (Figs. 3, 6) due to different depositional mechanisms (Beck et al., 2007). In Gulf of Corinth, combination magnetic foliation and the rock magnetic measurement s shows the boundaries between homogenites and overlying background sediments on selected examples (Campos et al., 2013). Coarse basal units represent deposition of clastic sediments that are transported by the head and body of a turbidity current. These sediments are detritus, containing high amount of Fe-bearing minerals and reworked Ca- and Sr-bearing fossil fragments (Fig. 6). In particular, the transition between coarse basal and homogenite parts of the THUs are commonly enriched in Ca and Sr, indicating the presence of biogenic carbonate material remobilized from the shelf and upper slope of the Kumburgaz Basin (Figs. 1,2,6) (Eriş et al., 2012).

Coarse sandy basal parts of THUs in the sapropels have thick laminations and commonly show undulated base contact indicating erosional contact with underlying background sediments (Fig. 6B). In lower sapropelic unit, marine sediments possess lower ARM_{30}/ARM, which are likely related to magnetic grain size variation and/or occurrence of greigite,. THU units have comparatively higher ARM_{30}/ARM In the lower sapropel, the average foliation of the background sediment is not systematically lower, and even sometime higher, than that of the homogenites, but the higher variability of the foliation parameter in the laminated sediment at the 2 cm sampling scale still allows making a distinction (Figs. 3,

5).Homogenites in the sapropels are rather thick (up to 80 cm) (Figs. 3,6; Table 2), and show darker shade than the background sediments in most radiographic images and photography (Figs. 3, 6B). Moreover, the χ_m is an additional proxy to mark the upper boundary in sapropelic THUs (Figs. 3,6) with both χ_m and foliation, showing a sharp decrease at the boundary between these units, as previously documented by Campos et al. (2013).

Basal parts of THUs in the lacustrine unit are commonly thicker and coarser than those of THUs in the sapropels and the upper marine unit (Fig. 6C). As in the THUs in the upper marine and sapropel units, these coarse basal parts are represented by high Sr counts generated by platy biogenic carbonate material (Fig. 6). ARM_3/ARM, SIRM and χ_m values in the lacustrine interval are in average larger than in the other facies (Fig. 3), but also display a high variability, while values in the homogenite remain homogeneous (Fig. 6). The lacustrine facies presents the sharpest foliation contrast at the top of homogenites, typically 1.06 to 1.02 across the boundary between the homogenite and the background sediment.

In summary, coarse basal parts of the THUs have more ferromagnetic particles than the homogenites and background sediments (Fig 6), suggesting that the magnetic signature is mainly controlled by the depositional environments (Fig. 5). The homogenite tends to be relatively homogenous in magnetic properties as in chemistry. However, the diagenesis plays an important role on magnetic grain size, as exposed by the variability of ARM_{30}/ARM values of the THUs (see sapropelic and lacustrine THU example in Figs. 6). The variability as a function of facies is higher for the background sediment than for the homogenites. As a result the ARM_{30}/ARM is lower in the background sediment than in the homogenites within the lower (laminated) sapropel facies, while the opposite is observed in the lacustrine facies (Figs. 3-6). SIRM and χ_m are also higher in the lacustrine background sediment indicating a higher content in ferromagnetic minerals. The sharpest contrast in magnetic properties and fabric between homogenites and background sediment is observed within the lacustrine interval.

Similarly, distinct boundary between THUs and the background sedimentation are observed on Alpine lakes (Crouzet et a., 2019). On the other hand, contrast is minimal, or reversed, within the laminated sapropel interval. These observations suggest that magnetic mineralogy and/or grain size is one of the factors influencing the magnetic fabric. Yet, in Sea of Marmara, variations in magnetic foliation in THUs are related to the deposition from turbulent flows rather than the magnetic mineralogy of the sediments (Campos et al., 2013). Homogenite units are deposited from suspension clouds following the deposition of the coarse basal layers from a body of turbulent flow, and differ from the overlying background sediment by having more homogeneous and compact textures and higher density (Shiki et al., 2000; Beck et al., 2007; Eriş et al., 2012; Polonia et al., 2013, 2017; Drab et al., 2015b; Van Daele et al., 2017; Yakupoğlu et al., 2019). Absence of bioturbation may also be a factor as the laminated sapropel appear to have relatively high (and highly heterogeneous) average magnetic foliation. Similarly, thick homogenites in lacustrine and marine non-sapropel facies should be less affected by bioturbation than background sediments and this could, regardless of mineralogy and depositional processes, favor a contrast in magnetic fabric.

5.3. Climatic and Hydrological Controls on Turbidite-Homogenite Frequency and Thickness

In general, the occurrence interval (or event frequency) and thickness of THUs in different chronostratigraphic units are highly variable (Fig. 3; Table 2; Supplementary Table 1). The occurrence interval ranges from an average of 114 yrs in the upper sapropel to 235 yrs in the lacustrine unit. Since we discarded the muddy hyperpycnal turbidites that may have been triggered by floods and storm waves, the remaining THU units, with a coarse and laminated basal part and a homogenous muddy upper part (homogenite), could be triggered by earthquake shaking in the tectonically active SoM basins (Fig. 3) (e.g. see Çağatay et al., 2012; McHugh et al., 2014; Drab et al., 2015b; Yakupoğlu et al., 2019).

Comparison of two piston cores (CS-01 and CS-14), which are ~ 2.5 km apart in the Kumburgaz Basin, show that THUs in Late Holocene period are rather similar in terms of THU event frequency, thickness and grain-size. However, the numbers of THUs deposited in the last 6 kyrs in the two cores are different; CS-01 and CS-14 contain 28 and 34 THUs respectively, which correspond to average recurrence intervals of 220 and 150 years, respectively (Fig. 2). Moreover, different units in core CS-14 has widely variable THU occurrence intervals, with the individual event intervals ranging from 37 to 1200 years (Supplementary Table 1). If it is presumed that these units are triggered with earthquakes, this high variability is inconsistent with the 200-250 yrs recurrence interval of historical Mw>7 earthquakes in the Marmara region (e.g., Ambraseys and Finkel, 1995; Parsons, 2004). THUs also show different thicknesses in different units of core CS-14 succession. These observations suggest that factors other than earthquake magnitude need to be considered in order to explain the temporal and spatial variability of THU occurrence and thickness in a given basin (e.g. Wilhelm et al., 2016, Ikehara et al., 2016, 2017, 2020). These include core location in relation to the basin morphology, sedimentation rate, sediment sensitivity to earthquake shaking, and sea level change and related paleoenvironmental changes.

The basin depo-centers are assumed to be the best locations for a complete THU record, potentially comprising the highest THUs thicknesses of gravity-driven sedimentary deposits (McHugh et al., 2006, 2014; Goldfinger, 2011; Patton et al., 2015). However, the difference in the number of THU units and average THU occurrence intervals between cores CS-01 and CS-14 in the Kumburgaz Basin can be explained by their accessibility to the sediment transport routes rather than the water depth (Figs. 1, 2). Core CS-01 is recovered at -834 m near the toe of the north eastern canyon (Fig. 1), whereas core CS-14 is recovered at -820 m near the basin center on a structural high between two depo-centers. Its central position in the basin, together with its accessibility to sediment input from both the northeastern and

northern canyons and possibly the northwestern canyon, makes the location of core CS-14 ideal for recording the maximum number of turbidites (Figs. 1, 2). The common presence of several amalgamated turbidites in core CS-14 supports sediment transport and deposition by turbidity currents arriving from the two or three canyons (Supplementary Table 1).

Other factors, such as intensity of earthquake shaking, sedimentation rate, sensitivity of the sediments to remobilization, and environmental factors (e.g. climate, sea/lake level, salinity changes), appear to be important in THU frequency and thickness variations. In particular, earthquake epicenter and magnitude, and the distribution of strong-motion parameters (e.g. the peak ground acceleration: PGA) are believed to be important for generating turbidity flows (e.g. Howarth et al. 2021 and references therein). Short average event intervals (e.g. average: 114 yrs in upper sapropel of core CS14) suggest that the earthquake magnitude threshold for triggering turbidity currents may not be only limited to large events if there are efficient sediment transport routes such as the steep northern slope (with up to 20-degree slope angles) and canyon systems in the Kumburgaz Basin (Fig 1). This assertion is supported by the occurrence of the turbidity currents triggered by the Mw 5.8 earthquake of Sept 26, 2019 in the NE corner of the Central Basin (Henry et al., 2022). This raises the question if a remote but strong earthquake, not necessarily in submerged context, may also trigger turbidites and recorded in the sedimentary sequence. However, subaqueous paleoseismological data from the Sea of Marmara (SoM) (e.g., Çağatay et al., 2012; Drab et al., 2012, 2015b; McHugh et al., 2015) and historical earthquake data (e.g., Ambraseys, N.N., Finkel, C.F., 1995) suggests that ground acceleration generated by onshore M=6-7.4 earthquakes east and south of the SoM with epicenters more than ca. 50 km of the basins did not trigger turbidites. For example, some earthquakes (e.g. 25 May 1719 earthquake with Ms=7.4 and 1754 earthquake with Ms=6.8 with epicenters east of the İzmit Gulf) were not

recorded in the sediments of the Karamürsel Basin in the İzmit Gulf (Çağatay et al., 2012, p.356 and references therein).

The THU occurrence interval and thickness distribution in core CS-14 also indicates the importance of environmental and hydrological factors such as sea level, sedimentation rate and salinity changes. The lacustrine unit contains the thickest and coarsest (coarse sand in basal parts) THUs in the core lithology with an average thickness of 20.8 cm and an event frequency of 4.255 $kyrs^{-1}$ (i.e. average event interval: 241 yrs) (Table 2). It is also characterized by the highest total sedimentation rate (1.98 mm/yr) and lowest TB-TT thickness ratio of 0.3, with THUs forming 53% of the unit's thickness (Table 2; Supplementary Table 1). THU thickness in the unit, calculated as five-point moving average, decreases from 38 cm from 14.6 kyrs BP to 8.5 cm before the sapropel deposition at 11.2 krs BP (Fig. 7A). A parallel change occurs in THU fraction, calculated as five-point moving average of each THU thickness divided by total sediment thickness between two events, as well as in the event interval (Fig 7B, C); the THU fraction ranges up to 73 % in the lower part of the lacustrine unit, but decreases to 35 % in the upper part of the lacustrine unit and in the marine unit below the lower sapropel and the five-point moving average event interval changes from ~250 yrs to 95 years (Fig. 7C). The high sediment input in the Kumburgaz basin during the Late Glacial period can be explained by the fact that, water level of the Marmara "lake" was below the Dardanelles Strait's sill depth, but gradually increase to -85 m just before the marine reconnection at ~12.6 kyrs BP (Figs. 1,3,4) (Çağatay et al., 2003; 2015; Eriş et al., 2011). Hence, the shelf was largely exposed during the deposition of the lacustrine unit until ~13.5 kyrs and fluvial sediment input from the Büyük Çekmece drainage network was directly delivered to the shelf edge and slope en route to the deep basin by gravity flow deposits. However, a decrease in the sediment input occurred during the 13.5-12.6 ka BP, which is likely to be due to a lake level increase.

Slope instability may have been another likely factor for THU events during the lacustrine period. Based on Cl^-, O and H isotope analyses of pore waters and a transport model, Aloisi et al. (2015) estimated the salinity of ~4 psu for the Marmara "lake" waters before the marine reconnection. Under such lacustrine fresh-brackish conditions together with low sea level provides hydrostatic pressure change on sediments, which deposited along the canyon and basin slopes would have been relatively unstable and may have further contributed to the thick THU deposition and low TB-TT thickness ratio in the Kumburgaz Basin.

After the full marine connection at 12.6 kyrs BP, the salinification of the SoM deep water was rapid, reaching the present levels within 1-2 kyrs of the connection (Çağatay et al., 2009; Aloisi et al., 2015), which possibly contributed to the stability of the slopes and reducing the canyon activity. The lower sapropel was deposited during 11.2-5.7 kyrs interval. The sea level rose from -85 m at 12.6 kyrs BP to the present sea level ~6 kyrs BP, before the end of the lower sapropel deposition (Grant et al., 2012). The total sedimentation rate was relatively high (1.68 mm/yr) with the THUs forming 35% of the sapropel thickness. High sedimentation rate for this period could have resulted from: (1) a wet and warm climatic condition with a high fluvial input (Caner and Algan, 2002; Mudie et al., 2002; Valsecchi et al., 2012), and (2) salinity-derived flocculation of clay-size fluvial material (Gibb, 1983; Wilkinson et al., 1997). However, this process is expected to enhance clay settling near river-marine water mixing zones, but with the relatively lower sea level, the mixing zone close to the shelf edge and a larger flux of hemipelagic sediment was settling out of suspension in the basin.

The lower sapropel includes relatively thick THUs with an average thickness of 15.7 cm and average TB-TT thickness ratio of 0.6 (Supplementary Table 1). THUs in this unit were deposited with the lowest frequency of 3.484 events $kyrs^{-1}$ (i.e. longest average event

interval of 287 yrs) in the sequence (Table 2; Supplementary Table 1). Five-event moving average THU thickness in this unit ranges between ~40 cm and 6 cm, while average fractional thickness varies between 20 % and 40 %, with a decrease in both parameters towards the top of the unit (Fig. 7A, B). The THU event interval is ~700 years for the main part of the unit but decreases to ~150 years in the upper quarter part (Fig. 7C). Hence, the THU fraction in the lower sapropel is much lower and the THU event interval is considerably longer than those in the lacustrine unit. Moreover, the basal parts of THUs within the lower sapropel are finer in grain size and TB-TT thickness ratio is higher than that of THUs of the lacustrine unit.

The main control on the long event interval and grain size of THUs in most part of the lower sapropel appears to be the cohesive and relatively high shear strength of sapropels, which result from particle bonding between the organic matter and in situ organic and clay fabrics that develop by deposition from anoxic water column (Kopf et al., 1998; Obuka et al., 2015). Such geomechanical properties would require a relatively large earthquake shaking (strong-ground motion) to trigger turbidity currents from the basin slopes. Long intervals between the turbidite events in turn allowed thick sediment accumulation (sediment loading) on the slope and shelf edge, which was consequently remobilized by earthquake shaking, resulting in the relatively thicker THUs, with relatively higher TB-TT thickness ratios in the sapropel unit. This conclusion is supported by similar trends of the THU thickness and event interval profiles for almost the entire core section (Fig 3; Table 2).

The rising sea level was stabilized towards the end of the lower sapropel deposition, and the sedimentation rate, THU thickness, and event recurrence interval decreased, and the TB-TT thickness ratio increased towards end of the upper sapropel deposition and during the ensuing marine (5.7-5.4 kyrs BP), upper sapropel (5.4-2.7 kyrs BP) and recent marine (2.7 kyrs BP to present) depositional intervals (Fig. 7A, C; Table 2; Supplementary Table 1). The transition to low sedimentation rates and gradual increase in the TB-TT thickness ratio

starting from ~7 kyrs BP was mainly due to rise in sea level (Fig. 4), which caused most fluvial sediments to be trapped in the Büyük Çekmece Lagoon and near coastal areas, rather than reaching to the shelf edge, slope and basinal areas. Only small amounts of fine sediments would have been transported by currents to accumulate on the slopes, and subsequently mobilized en route to the basin to be deposited as thin (6-7 cm-thick) and largely muddy THUs at high frequency in the upper sapropel and latest marine units, as indicated also by the relatively low TB-TT thickness ratio (Fig 3, Table 2; Supplementary Table 1). Indeed, the frequency of THU occurrence in the two units, and in particular in the upper sapropel, is higher than the underlying lower sapropel and lacustrine units. This is mainly due to the sensitivity of these marine sediments to earthquake shaking because of their lower TOC content, compared to that of the lower sapropel, and to their deposition under high sea level, compared to the lake level during the deposition of the lacustrine unit.

The upper sapropel and the recent marine unit show some fluctuations in the turbidite thickness, turbidite fraction and event interval (Fig. 7), which are likely due to artefacts in the age model (e.g. two radiocarbon ages in a short interval). However, some differences may be related to environmental conditions; upper sapropel was deposited with slightly higher organic productivity and under relatively lower bottom-water oxygen conditions than the recent marine unit, as indicated by the TOC and Mn profiles (Fig. 4). These differences are reflected in the relatively higher total and background sedimentation rates, lower TB-TT thickness ratio and shorter average event interval of the upper sapropel unit than those of the recent marine unit (Table 2).

6. Conclusions

Geochemical and rock magnetic parameters of core CS-14 from Kumburgaz basin enable us to provide a more accurate determination of the THU boundaries within the last 15 kyrs BP. THUs deposited in marine (including Holocene sapropels) and lacustrine facies of the core

show different characteristics in terms of thickness, grain size, geochemical and magnetic aspects. These differences are mainly related to the sensitivity of sediments to remobilization, core location and hydrological conditions related to both the sea level and salinity rise subsequent to the full marine connection of the SoM. In 15 kyrs-long sedimentary record includes different lacustrine and marine, including Holocene sapropels, are characterized by lithological and geochemical precursors (TOC, µ-XRF). A robust event-free age-depth model was constructed to date the units and determine the frequency (event interval) of THUs.

Boundaries between homogenites and overlying background sediments are well-defined by *AMS* (magnetic foliation). The magnetic foliation shows strong positive pulses in THUs in every facies indicating that its trend is related to the changes in depositional setting and to the rising sea level rather than the magnetic signature of THUs and hemipelagites. Based on the age-depth model of the core, average THU occurrence intervals in marine (2.7 kyrs BP-present), upper sapropel (5.4-2.7 kyrs BP), lower sapropel (11.2-5.7 kyrs BP), marine (12.6-11.2 kyrs BP) and lacustrine units (15-12.6 kyrs BP) are ~160 yrs, ~114 yrs, ~287 yrs, 246 yrs and ~235 yrs, respectively.

Results of this study enhance our understanding of turbidite generation and its use in subaqueous paleoseismology. Short THU intervals of upper sapropel and the most recent marine sequence suggest the possibility of turbidity current triggering and THU deposition by moderate magnitude earthquakes (5-6.5 Ms). Several environmental factors (climatic and hydrological), together with seismic activity, affect the deposition of THUs, and should be considered in subaqueous paleoseismological studies. In particular, sensitivity of sediments to remobilization during earthquake shaking, together with hydrological (sea level and salinity), changes are considered to be of critical importance in understanding the conditions of turbidite generation, and therefore, in paleoseismological studies in the Sea of Marmara and similar marine/lacustrine settings.

Data Availability

Global sea level dataset related to this article can be found at https://doi.org/10.1038/nature11593 an open-source online data repository hosted at https://www.nature.com/articles/nature11593#Sec3 (Grant et al., 2012).

All sediment core datasets related to this article can be found at http://www.emcol.itu.edu.tr/Icerik.aspx?sid=13881 an online data repository.

Acknowledgments

This study is part of Nurettin Yakupoğlu's PhD Dissertation. Cores were taken during MARSITECRUISE of Ifremer/Genavir R.V.Pourquoi Pas?, within the framework of MARSITE FP7 EU Project (grant agreement no.: 308417). Financial support was provided by the bilateral ANR/TUBITAK collaborative research project MAREGAMI (ANR-16-CE03-0010-02 and Tubitak Project 116Y371). Part of this work has been supported by TÜBİTAK 1002 project (118Y057) and ITU BAP project (MDK-2020-42743). All geochemical and sedimentological analyses were performed in ITU EMCOL laboratories.

References

Adams, J., 1990. Paleoseismicity of the Cascadia subduction zone: evidence from turbidites off the Oregon-Washington margin. Tectonics 9 (4), 569–583.

Akinyemi, F. O., Hutchinson, S. M., Mîndrescu, M., & Rothwell, J. J. 2013. Lake sediment records of atmospheric pollution in the Romanian Carpathians. Quaternary International, 293, 105-113.

Aloisi, G., Soulet, G., Henry, P., Wallmann, K., Sauvestre, R., Vallet-Coulomb, C., Bard, E., 2015. Freshening of the Marmara Sea prior to its post-glacial reconnection to the

Mediterranean Sea. Earth Planet. Sci. Lett. 413, 176–185. http://dx.doi.org/10.1016/j.epsl.2014.12.052.

Alp, H. 2014. Evidence for active faults in Küçükçekmece Lagoon (Marmara Sea, Turkey), inferred from high-resolution seismic data. Geo-Marine Letters, 34(5), 447-455.

Ambraseys, N.N., Finkel, C.F., 1995. The Seismicity of Turkey and Adjacent Areas - A Historical Review. Eren Yayıncılık, Istanbul, pp. 1500–1800. 240 pp.

Armijo, R., Meyer, B., Navarro, S., King, G., & Barka, A. 2002. Asymmetric slip partitioning in the Sea of Marmara pull-apart: A clue to propagation processes of the North Anatolian fault?. Terra Nova, 14(2), 80-86.

Ikehara, K., Irino, T., Usami, K., Jenkins, R., Omura, A., & Ashi, J. (2014). Possible submarine tsunami deposits on the outer shelf of Sendai Bay, Japan resulting from the 2011 earthquake and tsunami off the Pacific coast of Tohoku. Marine Geology, 358, 120-127.

Avşar, U., Hubert-Ferrari, A., De Batist, M., Schmidt, S., Fagel, N., 2015. Sedimentary records of past earthquakes in Boraboy Lake during the last ca 600 years (North Anatolian Fault, Turkey). Palaeogeography, Palaeoclimatology, Palaeoecology 433, 1–9.

Aydoğdu, A., Hoar, T. J., Vukicevic, T., Anderson, J. L., Pinardi, N., Karspeck, A., ... & Özsoy, E. 2018. OSSE for a sustainable marine observing network in the Sea of Marmara. Nonlinear Processes in Geophysics, 25(3), 537-551.

Barnes, P.M., Bostock, H.C., Neil, H.L., Strachan, L.J., Gosling, M., 2013. A 2300-year Paleoearthquake record of the Southern Alpine Fault and Fiordland Subduction Zone, New Zealand, based on stacked turbidites. Bulletin of the Seismological Society of America 103 (4), 2424–2446.

Beck, C. 2009. Late Quaternary lacustrine paleo-seismic archives in north-western Alps: Examples of earthquake-origin assessment of sedimentary disturbances. Earth-Science Reviews, 96(4), 327-344.

Beck, C., de Lépinay, B. M., Schneider, J. L., Cremer, M., Çağatay, N., Wendenbaum, E., ... & Jaouen, A. 2007. Late Quaternary co-seismic sedimentation in the Sea of Marmara's deep basins. Sedimentary Geology, 199(1-2), 65-89.

Beck, C., Manalt, F., Chapron, E., Van Rensbergen, P., De Batist, M., 1996. Enhanced seismicity in the early post-glacial period: evidence from the post-würm sediments of Lake Annecy, Northwestern Alps. Journal of Geodynamics 22, 155-171.

Beşiktepe, Ş.T., Sur, H.I., Özsoy, E., Latif, M.A., Oğuz, T., Ünlüata, Ü., 1994. The circulation and hydrography of the Marmara Sea. Progress in Oceanography 34 (4), 285–334.

Blaauw, M., 2010. Methods and code for 'classical' age-modelling of radiocarbon sequences. Quat. Geochronol. 5, 512e518.

Bloemendal, J., King, J. W., Hall, F. R., & Doh, S. J. 1992. Rock magnetism of Late Neogene and Pleistocene deep-sea sediments: Relationship to sediment source, diagenetic processes, and sediment lithology. Journal of Geophysical Research: Solid Earth, 97(B4), 4361-4375.

Bourry, C., Chazallon, B., Charlou, J.L., Donval, J.P., Ruffine, L., Henry, P., ... Moreau, M., 2009. Free gas and gas hydrates from the Sea of Marmara, Turkey: chemical and structural characterization. Chemical Geology 264 (1–4), 197–206.

Çağatay, M. N., & Uçarkuş, G. 2019. Morphotectonics of the Sea of Marmara: basins and highs on the North Anatolian continental transform plate boundary. In Transform plate boundaries and fracture zones (pp. 397-416). Elsevier.

Çağatay, M. N., Eriş, K. K., Makaroğlu, Ö., Yakupoğlu, N., Henry, P., Leroy, S. A., ... & Kende, J. 2019. The sea of Marmara during marine isotope stages 5 and 6. Quaternary Science Reviews, 220, 124-141.

Çağatay, M. N., Görür, N., Algan, O., Eastoe, C., Tchapalyga, A., Ongan, D., ... & Kuşcu, I. 2000. Late Glacial–Holocene palaeoceanography of the Sea of Marmara: timing of connections with the Mediterranean and the Black Seas. Marine Geology, 167(3-4), 191-206.

Çağatay, M.N., Algan, O., Sakınç, M., Eastoe, C., Egesel, L., Balkıs, N., Ongan, D., Caner, H., 1999. A mid-late Holocene sapropelic sediment unit from the Southern Marmara shelf and its Paleoenvironmental significance. Quaternary Science Reviews 18, 531–540.

Çağatay, M.N., Erel, L., Bellucci, L.G., Polonia, A., Gasperini, L., Eris, K., Sancar, Ü., Biltekin, D., Uçarkus, G., Ülgen, U.B., Damci, E., 2012. Sedimentary earthquake records in the Izmit Gulf, Sea of Marmara, Turkey. Sedimentary Geology 282, 347–359. https://doi.org/10.1016/j.sedgeo.2012.10.001.

Çağatay, M.N., Eriş, K., Ryan, W.B.F., Sancar, Ü., Polonia, A., Akçer, S., ... Bard, E., 2009. Late Pleistocene–Holocene evolution of the northern shelf of the Sea of Marmara. Marine Geology 265 (3–4), 87–100.

Çağatay, M.N., Görür, N., Polonia, A., Demirbağ, E., Sakınç, M., Cormier, M.H., ... Eriş, K., 2003. Sea-level changes and depositional environments in the Izmit Gulf, eastern Marmara Sea, during the late glacial–Holocene period. Marine Geology 202 (3–4), 159–173.

Çağatay, M.N., Wulf, S. Guichard, F. Özmaral, A., Henry, P, Gasperini, L., 2015. Tephra record from the Sea of Marmara for the last 71 ka and its paleoceanographic implications. Marine Geology, 361: 96-110.

Çağatay, N., Görür, N., Algan, O., Eastoe, C.J., Tchapalyga, A., Ongan, D., ... Kuscu, I., 2000. Late Glacial-Holocene paleoceanography of the Marmara Sea: timing of connections with the Mediterranean and the Black Seas. Marine Geology 167, 191–206.

Campos, C., Beck, C., Crouzet, C., Demory, F., Van Welden, A., & Eris, K. 2013. Deciphering hemipelagites from homogenites through anisotropy of magnetic susceptibility. Paleoseismic implications (Sea of Marmara and Gulf of Corinth). Sedimentary Geology, 292, 1-14.

Caner, H. and O. Algan, 2002. Palynology of sapropelic layers from the Marmara Sea. Marine Geology, 190: 35–46.

Chapron, E., Beck, C., Pourchet, M., & Deconinck, J. F. 1999. 1822 earthquake-triggered homogenite in Lake Le Bourget (NW Alps). Terra Nova, 11(2-3), 86-92.

Chiggiato, J., Jarosz, E., Book, J. W., Dykes, J., Torrisi, L., Poulain, P. M., ... & Beşiktepe, Ş. 2012. Dynamics of the circulation in the Sea of Marmara: numerical modeling experiments and observations from the Turkish straits system experiment. Ocean Dynamics, 62(1), 139-159.

Cita, M. B., & Rimoldi, B. 1997. Geological and geophysical evidence for a holocene tsunami deposit in the eastern Mediterranean deep-sea record. Journal of Geodynamics, 24(1-4), 293-304.

Cita,M.B., Aloisi, G., 2000. Deep-sea tsunami deposits triggered by the explosion of Santorini (3500 a BP), Eastern Mediterranean. Sedimentary Geology 135, 181–203.

Dalgıç, S. 2004. Factors affecting the greater damage in the Avcılar area of Istanbul during the 17 August 1999 Izmit earthquake. Bulletin of Engineering Geology and the Environment, 63(3), 221-232.

Demory, F., Nowaczyk, N. R., Witt, A., & Oberhänsli, H. 2005a. High-resolution magnetostratigraphy of late quaternary sediments from Lake Baikal, Siberia: timing of intracontinental paleoclimatic responses. Global and Planetary Change, 46(1-4), 167-186.

Demory, F., Oberhänsli, H., Nowaczyk, N. R., Gottschalk, M., Wirth, R., & Naumann, R. 2005b. Detrital input and early diagenesis in sediments from Lake Baikal revealed by rock magnetism. Global and Planetary Change, 46(1-4), 145-166.

Drab, L., Carlut, J., Hubert-Ferrari, A., Martinez, P., Lepoint, G., & El Ouahabi, M. 2015a. Paleomagnetic and geochemical record from cores from the Sea of Marmara, Turkey: Age constraints and implications of sapropelic deposition on early diagenesis. Marine Geology, 360, 40-54.

Drab, L., Hubert-Ferrari, A., Schmidt, S., Martinez, P., 2012. The earthquake record in the western part of the Sea of Marmara, Turkey. In: Pantosi, D. (Ed.), Natural Hazards and Earth System Sciences, Special Issue "Subaqueous Paleoseismology", pp. 1235–1254 https://doi.org/10.5194/nhess-12-2012.

Drab, L., Hubert-Ferrari, A., Schmidt, S., Martinez, P., Carlut, J., El Ouahabi, M., 2015b. Submarine earthquake history of the Çınarcık segment of the North Anatolian Fault in the Marmara Sea, Turkey. Bulletin of the Seismological Society of America 105 (2A), 622–645.

EIE, 1993. Sediment data and sediment transport amounts for surface waters in Turkish rivers. EIE, Ankara, Rep Gen. Dir. State Electric Serv. 93e59.

Eriş, K. K., Çağatay, M. N., Akçer, S., Gasperini, L., & Mart, Y. 2011. Late glacial to Holocene sea-level changes in the Sea of Marmara: new evidence from high-resolution seismics and core studies. Geo-Marine Letters, 31(1), 1-18.

Eriş, K. K., Ryan, W. B. F., Çağatay, M. N., Sancar, U., Lericolais, G., Menot, G., & Bard, E. 2007. The timing and evolution of the post-glacial transgression across the Sea of Marmara shelf south of Istanbul. Marine Geology, 243(1-4), 57-76.

Eriş, K. K., Sabuncu, A., Gasperini, L., Polonia, A., & Kındap, T. 2019. Influence of climate on the late Pleistocene depositional history of the Gulf of Gemlik (Sea of Marmara). Geo-Marine Letters, 39(3), 205-221.

Eriş, K.K., Çağatay, N., Beck, C., Mercier de Lepinay, B., Campos, C., 2012. Late-Pleistocene to Holocene sedimentary fills of the Cinarcik Basin of the Sea of Marmara. Sedimentary Geology 281, 151–165.

Filikci, B., Eriş, K. K., Çağatay, N., Sabuncu, A., & Polonia, A. 2017. Late glacial to Holocene water level and climate changes in the Gulf of Gemlik, Sea of Marmara: evidence from multi-proxy data. Geo-Marine Letters, 37(5), 501-513.

Flerit, F., Armijo, R., King, G. C. P., Meyer, B., & Barka, A. 2003. Slip partitioning in the Sea of Marmara pull-apart determined from GPS velocity vectors. Geophysical Journal International, 154(1), 1-7.

Franke, C., Kissel, C., Robin, E., Bonté, P., & Lagroix, F. 2009. Magnetic particle characterization in the Seine river system: Implications for the determination of natural versus anthropogenic input. Geochemistry, Geophysics, Geosystems, 10(8).

Gastineau, R., de Sigoyer, J., Sabatier, P., Fabbri, S. C., Anselmetti, F. S., Develle, A. L., ... & Gebhardt, A. C. 2021. Active subaquatic fault segments in Lake Iznik along the middle strand of the North Anatolian Fault, NW Turkey. Tectonics, 40(1), e2020TC006404.

Ge, S., Shi, X., Liu, Y., Wang, K., Zou, J., Diao, J., ... & Wang, C. 2012. Turbidite and bottom-current evolution revealed by anisotropy of magnetic susceptibility of redox sediments in the Ulleung Basin, Sea of Japan. Chinese Science Bulletin, 57(6), 660-672.

Gibbs, R.J., 1983. Coagulation rates of clay minerals and natural sediments. Journal of Sedimentary Research) 53 (4): 1193–1203. https://doi.org/10.1306/212F8341-2B24-11D7-8648000102C1865D.

Goldfinger, C., 2011. Submarine paleoseismology based on turbidite records. Annual Review of Marine Science 3, 35–66.

Goldfinger, C., Galer, S., Beeson, J., Hamilton, T., Black, B., Romsos, C., ... Morey, A., 2017. The importance of site selection, sediment supply, and hydrodynamics: a case study of submarine paleoseismology on the Northern Cascadia margin, Washington USA. Marine Geology 384, 4–46.

Goldfinger, C., Grijalva, K., Burgmann, K., Morey, A., Johnson, J.E., Nelson, C.H., Gutiérrez- Pastor, J., Karabanov, E., Patton, J., Gracia, E., 2008. Late Holocene rupture of the northern San Andreas Fault and possible stress linkage to the Cascadia Subduction Zone. Seismological Society of America, Bulletin 98, 861–899.

Goldfinger, C., Morey, A.E., Nelson, C.H., Gutierrez-Pastor, J., Johnson, J.E., et al., 2007. Rupture lengths and temporal history of significant earthquakes on the offshore and north coast segments of the northern San Andreas Fault based on turbidite stratigraphy. Earth and Planetary Science Letters 254, 9–27.

Goldfinger, C., Nelson, C.H., Johnson, J.E., 2003. Holocene earthquake records from the Cascadia subduction zone and northern San Andreas fault based on precise dating of offshore turbidites. Annual Review of Earth and Planetary Sciences 31, 555–577.

Gorsline, D. S., De Diego, T., & Nava-Sanchez, E. H. 2000. Seismically triggered turbidites in small margin basins: Alfonso Basin, western Gulf of California and Santa Monica Basin, California borderland. Sedimentary Geology, 135(1-4), 21-35.

Grant, K. M., Rohling, E. J., Bar-Matthews, M., Ayalon, A., Medina-Elizalde, M., Ramsey, C. B., Roberts, A. P. 2012. Rapid coupling between ice volume and polar temperature over the past 150,000 years. Nature, 491(7426), 744-747.

Gutiérrez-Pastor, J., Nelson, C.H., Goldfinger, C., Escutia, C., 2013. Sedimentology of seismo-turbidites off the Cascadia and northern California active tectonic continental margins, northwest Pacific Ocean. Marine Geology 336, 99–119.

Harrison, C. G. A., & Funnell, B. M. 1964. Relationship of palaeomagnetic reversals and micropalaeontology in two late Caenozoic cores from the Pacific Ocean. Nature, 204(4958), 566-566.

Henry, H., Özeren, M.S., Yakupoğlu. N., Cakir, Z., De Saint-Léger, E., De Gésincourt, O.D., Tengberg, A., Chevalier, C., Papoutsellis, C., Postacıoğlu, N. Dogan, U., Karabulut, K., Uçarkuş G., Çağatay, M.N. 2022. Slow build-up of turbidity currents triggered by a moderate earthquake in the Sea of Marmara. Natural hazards and Earth System Sciences. https://doi.org/10.5194/nhess-2021-323.

Hiscott, R. N., Hall, F. R., & Pirmez, C. 1997. Turbidity-current overspill from the Amazon Channel: texture of the silt/sand load, paleoflow from anisotropy of magnetic susceptibility, and implications for flow processes. In Proceedings-Ocean Drilling Program Scientific Results (pp. 53-78). NATIONAL SCIENCE FOUNDATION.

Howarth, J. D., Orpin, A. R., Kaneko, Y., Strachan, L. J., Nodder, S. D., Mountjoy, J. J., ... & Cağatay, M. N. 2021. Calibrating the marine turbidite palaeoseismometer using the 2016 Kaikōura earthquake. Nature Geoscience, 14(3), 161-167.

Hrouda, F. 1982. Magnetic anisotropy of rocks and its application in geology and geophysics. Geophysical surveys, 5(1), 37-82.

Ikehara, K., Kanamatsu, T., Nagahashi, Y., Strasser, M., Fink, H., Usami, K., et al. 2016. Documenting large earthquakes similar to the 2011 Tohoku-oki earthquake from sediments deposited in the Japan Trench over the past 1500 years. Earth and Planetary Science Letters, 445, 48–56. doi:10.1016/j.epsl.2016.04.009.

Ikehara, K., Usami, K., Kanamatsu, T., Danhara, T., & Yamashita, T. 2017. Three important Holocene tephras off the Pacific coast of the Tohoku region, Northeast Japan: Implications for correlating onshore and offshore event deposits. Quaternary International, 456, 138–153. doi:10.1016/j.quaint.2017.08.022.

Ikehara, K., Usami, K., & Kanamatsu, T. (2020). Repeated occurrence of surface-sediment remobilization along the landward slope of the Japan Trench by great earthquakes. Earth, Planets and Space, 72(1), 1-9.

Jelinek, V. 1981. Characterization of the magnetic fabric of rocks. Tectonophysics, 79(3-4), T63-T67.

Johnson, H. P., Lowrie, W., & Kent, D. V. 1975. Stability of anhysteretic remanent magnetization in fine and coarse magnetite and maghemite particles. Geophysical Journal International, 41(1), 1-10.

Kastens, K., Cita, M.B., 1981. Tsunami-induced sediment transport in the abyssal Mediterranean Sea. Geological Society of America Bulletin 119, 151–165.

Kazancı, N., Leroy, S., Ileri, Ö., Emre, Ö., Kibar, M., & Öncel, S. 2004. Late Holocene erosion in NW Anatolia from sediments of Lake Manyas, Lake Ulubat and the southern shelf of the Marmara Sea, Turkey. Catena, 57(3), 277-308.

Kopf, A. Clennell, M.B. , Flecker, R. 1998. Relationship between the variation of undrained shear strength, organic carbon content, and the origin and frequency of enigmatic normal faults in fine-grained sediments from advanced piston cores from the eastern Mediterranean. In: Robertson, A.H.F., Emeis, K.-C., Richter, C., and Camerlenghi, A. (Eds.), Proceedings of the Ocean Drilling Program, Scientific Results, Vol. 160, Chapter 49, pp.655-661.

Kruiver, P. P., Kok, Y. S., Dekkers, M. J., Langereis, C. G., & Laj, C. 1999. A pseudo-Thellier relative palaeointensity record, and rock magnetic and geochemical parameters in relation to climate during the last 276 kyr in the Azores region. Geophysical Journal International, 136(3), 757-770.

Le Pichon, X., Şengör, A. M. C., Demirbağ, E., Rangin, C., Imren, C., Armijo, R., ... & Tok, B. 2001. The active main Marmara fault. Earth and Planetary Science Letters, 192(4), 595-616.

Major, C. O., Goldstein, S. L., Ryan, W. B., Lericolais, G., Piotrowski, A. M., & Hajdas, I. 2006. The co-evolution of Black Sea level and composition through the last deglaciation and its paleoclimatic significance. Quaternary Science Reviews, 25(17-18), 2031-2047.

McClusky, S., Balassanian, S., Barka, A., Demir, C., Ergintav, S., Georgiev, I., ... & Veis, G. 2000. Global Positioning System constraints on plate kinematics and dynamics in the eastern Mediterranean and Caucasus. Journal of Geophysical Research: Solid Earth, 105(B3), 5695-5719.

McHugh, C.M., Braudy, N., Çağatay, M.N., Sorlien, C., Cormier, M.H., Seeber, L., Henry, P., 2014. Seafloor fault ruptures along the North Anatolia Fault in the Marmara Sea, Turkey: link with the adjacent basin turbidite record. Marine Geology 353, 65–83.

McHugh, C.M., Seeber, L., Braudy, N., Cormier, M.-H., Davis, M.B., Diebold, J.B., Dieudonne, N., Douilly, R., Gulick, S.P.S., Hornbach, M.J., Johnson III, H.E., Ryan, K.M.,

Sorlien, C.C., Steckler, M.S., Symithe, S.J., Templeton, J., 2011. Offshore sedimentary effects of the 12 January 2010 Haiti earthquake. Geology 39, 723–726.

McHugh, C.M.G., Seeber, L., Cormier, M.-H., Dutton, J., Çağatay, N., Polonia, A., Ryan, W.B.F., Görür, N., 2006. Submarine earthquake geology along the North Anatolia Fault in the Marmara Sea, Turkey: a model for transform basin sedimentation. Earth and Planetary Science Letters 248, 661–684.

Moernaut, J., Van Daele, M., Heirman, K., Fontijn, K., Strasser, M., Pino, M., ... & De Batist, M. 2014. Lacustrine turbidites as a tool for quantitative earthquake reconstruction: New evidence for a variable rupture mode in south central Chile. Journal of Geophysical Research: Solid Earth, 119(3), 1607-1633.

Moernaut, J., Van Daele, M., Strasser, M., Clare, M. A., Heirman, K., Viel, M., ... & De Batist, M. 2017. Lacustrine turbidites produced by surficial slope sediment remobilization: a mechanism for continuous and sensitive turbidite paleoseismic records. Marine Geology, 384, 159-176.

Mudie, P.J., A. Rochon, and A.E. Aksu, 2002. Pollen stratigraphy of Late Quaternary cores from Marmara Sea: land–sea correlation and paleoclimatic history. Marine Geology, 190: 233–260.

Mulder, T., & Syvitski, J. P. 1995. Turbidity currents generated at river mouths during exceptional discharges to the world oceans. The Journal of Geology, 103(3), 285-299.

Nakajima, T., Kanai, Y., 2000. Sedimentary features of seismoturbidites triggered by the 1983 and older historical earthquakes in the eastern margin of the Japan Sea. Sedimentary Geology 135, 1–19.

Nemec, W. 1990. Aspects of sediment movement on steep delta slopes. Coarse-grained deltas, 10(2), 29-73.

Nizou, J., Demory, F., & Dubrulle-Brunaud, C. 2016. Monitoring of dredged-dumped sediment dispersal off the Bay of the Seine (northern France) using environmental magnetism. Comptes Rendus Geoscience, 348(6), 451-461.

Obuka, V. Šinka, M., Kļaviņš, M., Stankeviča, K., Korjakins, A., 2015. Sapropel as a Binder: Properties and Application Possibilities for Composite Materials. IOP Conf. Ser.: Mater. Sci. Eng. 96 012026. https://iopscience.iop.org/article/10.1088/1757-899X/96/1/012026.

Opdyke, N. D., Glass, B., Hays, J. D., & Foster, J. 1966. Paleomagnetic study of Antarctic deep-sea cores. Science, 154(3747), 349-357.

Parsons, T., 2004. Recalculated probability of M≥7 earthquakes beneath the Sea of Marmara. Journal of Geophysical Research., 109, doi:10.1029/2003JB002667.

Patton, J. R., Goldfinger, C., Morey, A. E., Ikehara, K., Romsos, C., Stoner, J., ... & Vizcaino, A. (2015). A 6600 year earthquake history in the region of the 2004 Sumatra-Andaman subduction zone earthquake. Geosphere, 11(6), 2067-2129.

Petersen, J., Wilhelm, B., Revel, M., Rolland, Y., Crouzet, C., Arnaud, F., ... & Magand, O. 2014. Sediments of Lake Vens (SW European Alps, France) record large-magnitude earthquake events. Journal of paleolimnology, 51(3), 343-355.

Polonia, A., Nelson, C.H., Romano, S., Vaiani, S.C., Colizza, E., Gasparotto, G., Gasperini, L., 2017. A depositional model for seismo-turbidites in confined basins based on Ionian Sea deposits. Marine Geology 384, 177–198.

Polonia, A., Panieri, G., Gasperini, L., Gasparotto, G., Bellucci, L.G., Torelli, L., 2013. Turbidite paleoseismology in the Calabrian Arc subduction complex (Ionian Sea).

Geochemistry, Geophysics, Geosystems 14, 112–140. https://doi.org/10.1029/2012GC004402.

Pouderoux, H., Lamarche, G., Proust, J.-N., 2012b. Building a 18 000-year-long paleoearthquake record from detailed deep-sea turbidite characterisation in Poverty Bay, New Zealand. Natural Hazards and Earth System Sciences 12, 1–25.

Pouderoux, H., Proust, J.N., Lamarche, G., Orpin, A., Neil, H., 2012a. Deep-sea sedimentation along the Hikurangi subduction margin (New Zealand) since the Last Glacial Maximum: characterisation, timing and origin of turbidites. Marine Geology 295e298, 51–76.

Pozza, M. R., Boyce, J. I., & Morris, W. A. 2004. Lake-based magnetic mapping of contaminated sediment distribution, Hamilton Harbour, Lake Ontario, Canada. Journal of Applied Geophysics, 57(1), 23-41.

Prior, D. B., Suhayda, J. N., Lu, N. Z., Bornhold, B. D., Keller, G. H., Wiseman, W. J., ... & Yang, Z. S. 1989. Storm wave reactivation of a submarine landslide. Nature, 341(6237), 47-50.

Provost, A.S., Chéry, J., Hassani, R., 2003. 3D mechanical modeling of the GPS velocity field along the North Anatolian fault. Earth and Planetary Science Letters 209 (3–4), 361–377.

Rapuc W., Sabatier P., Andric M., Crouzet C., Arnaud F., Smuc A., Chapron E., Develle A.-L., Wilhelm B., Demory F., Reyss J.-L., Régnier E., Daut G., Von Grafenstein U. 2018. Evolution of the local seismicity during the Holocene recorded in Bohinj's lacustrine sediments (Slovenia). *Sedimentology*, 65-5, 1777-1799. http://dx.doi.org/10.1111/sed.12446

Reilinger, R. E., McClusky, S. C., Oral, M. B., King, R. W., Toksoz, M. N., Barka, A. A., ... & Sanli, I. 1997. Global Positioning System measurements of present-day crustal movements

in the Arabia-Africa-Eurasia plate collision zone. Journal of Geophysical Research: Solid Earth, 102(B5), 9983-9999.

Reilinger, R., McClusky, S., Vernant, P., Lawrence, S., Ergintav, S., Cakmak, R., ... & Karam, G. 2006. GPS constraints on continental deformation in the Africa-Arabia-Eurasia continental collision zone and implications for the dynamics of plate interactions. Journal of Geophysical Research: Solid Earth, 111(B5).

Reimer, P. J., Bard, E., Bayliss, A., Beck, J. W., Blackwell, P. G., Ramsey, C. B., ... & Van Der Plicht, J. 2013. IntCal13 and Marine13 radiocarbon age calibration curves 0–50,000 years cal BP. radiocarbon, 55(4), 1869-1887.

Rochette, P., Jackson, M., & Aubourg, C. 1992. Rock magnetism and the interpretation of anisotropy of magnetic susceptibility. Reviews of Geophysics, 30(3), 209-226.

Ryan, W. B. 2007. Status of the Black Sea flood hypothesis. In The Black Sea Flood Question: Changes in Coastline, Climate, and Human Settlement (pp. 63-88). Springer, Dordrecht.

Sarı, E., Çağatay,M.N., 2006. Turbidities and their association with past earthquakes in the deep Çınarcık Basin of the Marmara Sea. Geo-Marine Letters 26, 69–76.

Şengör, A. M. C., Tüysüz, O., Imren, C., Sakınç, M., Eyidoğan, H., Görür, N., ... & Rangin, C. 2005. The North Anatolian fault: A new look. Annu. Rev. Earth Planet. Sci., 33, 37-112.

Shiki, T., Kumon, F., Inouchi, Y., Kontani, Y., Sakamoto, T., Tateishi, M., Matsubara, H., Fukuyama, K., 2000. Sedimentary features of the seismo-turbidites, Lake Biwa, Japan. Sedimentary Geology 135, 37–50.

Siani, G., Paterne, M., Arnold, M., Bard, E., Métivier, B., Tisnerat, N., & Bassinot, F. 2000. Radiocarbon reservoir ages in the Mediterranean Sea and Black Sea. Radiocarbon, 42(2), 271-280.

Stachowska, A., Łoziński, M., Śmigielski, M., Wysocka, A., Jankowski, L., & Ziółkowski, P. 2020. Anisotropy of magnetic susceptibility as an indicator for palaeocurrent analysis in folded turbidites (Outer Western Carpathians, Poland). Sedimentology, 67(7), 3783-3808.

Stoner, J. S., & St-Onge, G. 2007. Chapter three magnetic stratigraphy in paleoceanography: reversals, excursions, paleointensity, and secular variation. Developments in Marine Geology, 1, 99-138.

Straub, C., Kahle, H. G., & Schindler, C. 1997. GPS and geologic estimates of the tectonic activity in the Marmara Sea region, NW Anatolia. Journal of Geophysical Research: Solid Earth, 102(B12), 27587-27601.

Tamaki, M., Suzuki, K., & Fujii, T. 2015. Paleocurrent analysis of Pleistocene turbidite sediments in the forearc basin inferred from anisotropy of magnetic susceptibility and paleomagnetic data at the gas hydrate production test site in the eastern Nankai Trough. Marine and Petroleum Geology, 66, 404-417.

Tarling, D., & Hrouda, F. (Eds.). 1993. Magnetic anisotropy of rocks. Springer Science & Business Media.

Tolun, T., Çağatay, M.N., Carrigan, W.J., 2002. Organic geochemistry and origin of Holocene sapropelic layer and associated sediments in Marmara Sea. Marine Geology 190, 47–60.

Uçarkuş, G., 2010. Active Faulting and Earthquake Scarps a Long the North Anatolian Fault in The Sea of Marmara (Doctoral dissertation, Avrasya Yer Bilimleri Enstitüsü).

Ünlülata, Ü., Oğuz, T., Latif, M.A., Özsoy, E., 1990. On the physical oceanography of the Turkish Straits. The Physical Oceanography of Sea Straits. Springer, Dordrecht, pp. 25–60.

Valsecchi, V., M.F. Sánchez-Goñi, and L. Londeix, 2012. Vegetation dynamics in the Northeastern Mediterranean region during the past 23 000 yr: insights from a new pollen record from the Sea of Marmara. Clim. Past, 8: 1941–1956.

Van Daele, M., Meyer, I., Moernaut, J., De Decker, S., Verschuren, D., & De Batist, M. 2017. A revised classification and terminology for stacked and amalgamated turbidites in environments dominated by (hemi) pelagic sedimentation. Sedimentary Geology, 357, 72-82.

Vidal, L., Ménot, G., Joly, C., Bruneton, H., Rostek, F., Çağatay, M.N., Major, M., Bard, E., 2010. Hydrology in the Sea of Marmara during the last 23 ka: implications for timing of Black Sea connections and sapropel deposition. Paleoceanography 25 (1), pa1205. http://dx.doi.org/10.1029/2009pa001735

Wilhelm, B., Nomade, J. , Crouzet, C. , Litty, C., Sabatier, P., Belle, S., Rolland, Y., Revel, M., Courboulex, F., Arnaud, F., Anselmetti, F.S., 2016. Quantified sensitivity of small lake sediments to record historic earthquakes: Implications for paleoseismology, J. Geophys. Res. Earth Surf., 121, 2–16, http://doi:10.1002/2015JF003644.

Wilkinson, K.J. Negre, J.-C., Buffle, J. 1997. Coagulation of colloidal material in surface waters: the role of natural organic matterm Journal of Contaminant Hydrology. 26 (1–4), 229-243.

Wils, K., Van Daele, M., Kissel, C., Moernaut, J., Schmidt, S., Siani, G., & Lastras, G. 2020. Seismo-Turbidites in Aysén Fjord (Southern Chile) Reveal a Complex Pattern of Rupture Modes Along the 1960 Megathrust Earthquake Segment. Journal of Geophysical Research: Solid Earth, 125(9), e2020JB019405.

Yakupoğlu, N., Uçarkuş, G., Eriş, K. K., Henry, P., & Çağatay, M. N. 2019. Sedimentological and geochemical evidence for seismoturbidite generation in the Kumburgaz Basin, Sea of Marmara: Implications for earthquake recurrence along the Central High Segment of the North Anatolian Fault. Sedimentary Geology, 380, 31-44.

Figure Captions

Fig. 1. A) High resolution multi-beam bathymetry map of the Sea of Marmara (west to east; TB: Tekirdağ Basin, WH: Western High, CB: Central Basin, KB: Kumburgaz Basin, CH: Central High, CiB; Çınarcık Basin, GI: Gulf of İzmit) (Revised from Uçarkuş, 2010). Black lines represent the active faults. White box indicates the location of the Kumburgaz Basin and the inset map. B) Close up of bathymetry map of Kumburgaz Basin. Black lines indicate the active faults. Thick black line and yellow dots represents the CHIRP profile (P02) and core locations of CS-01 (Yakupoğlu et al., 2019) and CS-14 (this study) respectively. Note that northern canyons are indicated as following: NEC: North Eastern Canyon, NE: Northern Canyon, NWC: North Western Canyon.

Fig. 2. CHIRP profile (P02) from the Kumburgaz Basin, showing the main depositional units along the basin floor. Lacustrine-Marine transition (12.6 kyrs BP; Çağatay et al., 2015) is shown in blue line. Core CS-01 is located at depocenter covering the last 6 kyrs BP sedimentary records (Yakupoğlu et al., 2019) and Core CS-14 penetrates through lacustrine units of SoM up to 15 cal kyrs BP (Figs. 3, 4).

Fig. 3. Generalized lihological log of the core CS-14, showing the main lithostratigraphy photography and radiography of the marine and lacustrine units deposited during the last ~15 cal ka BP (Fig. 4). 70 turbidite layers are differentiated based on sedimentological, geochemical and magnetic precursors. Legend below shows different lithological units and symbols.

Fig. 4. Age-depth model of the core CS-14. Summarized sedimentary log shows the main lithostratigraphy of the marine and lacustrine units and TOC concentrations of the first 18 m. Age-depth model of the background sediments of the core CS-14 are reconstructed based on four ^{14}C ages and the age of a major lithological change (L-M transition) by using Clam.r Script (Blauuw, 2010). Red line represents the mean age of the iterations. Green, blue and red dots are the levels of the ^{14}C samples, L-M transition respectively. Gray overlay indicates the probability distribution. Mn profile and χ_m profiles are marked in red and blue color respectively. Background sedimentation rates are indicated according to each facies. The rightmost column indicates the climatic phases and global sea level curve of the last 12 kyrs BP (Grant et al., 2012).

Fig. 5. Summarized sedimentary log of the core accompanied with magnetic foliation, magnetic lineation, S ratio, SIRM, ARM_{30}/ARM profiles of 98 samples showing the rock magnetism proxies.

Fig. 6. Radiography and multi-parameter analyses (left to right; ARM_{30}/ARM, S ratio, gamma density, Mn, magnetic foliation and lineation, Ca, Sr, χ_m, Fe) of the selected THUs (THU-A, B, C) (see their positions on Fig 3). Green lines represent the boundary of THU units with background sediments.

Fig. 7. (A) THU thickness variation, (B) Variation of THU thickness fraction, calculated as each THU thickness divided by total sediment thickness between two events, (C) Variation of THU event interval.

Table 1. Summary of Accelerated Mass Spectrometry ^{14}C ages obtained from core CS-14 and the referenced age of full L-M transition (Çağatay et al., 2015). Reservoir correction for

Accelerated Mass Spectrometry dates applied as ~390 ± 85 yrs for marine according to Siani et al. (2000) and ~900 ± 100 yrs for lacustrine (Çağatay et al., 2015).

Sample ID	Depth (cm)	Uncalibrated Age (BP)	Calibrated Ages (BP)	Material
TÜBİTAK-675	52	2552±53	1608±219	benthic & planktonic foraminifera, echinoderm spicules
TÜBİTAK-676	92	2432±32	1752±236	benthic & planktonic foraminifera, echinoderm spicules
TÜBİTAK-678	554	5115±40	5028±241	benthic & planktonic foraminifera, echinoderm spicules
TÜBİTAK-794	1984	12538±51	14021±150	Bivalves
Lacustrine-Marine Transition	1740		12600±350 (Çağatay et al., 2015)	

Table 2. THU intervals, frequencies and thicknesses over the lithological facies. Extended list of each unit is displayed on Supplementary Table 1. Note that, standard deviation of THU intervals and thicknesses are indicated in parenthesis.

Unit/Facies	THU intervals (yrs)	THU frequency (kyrs-1)	Background Sedimentation Rate (mm/yr)	Total Sedimentation Rate (mm/yr)	THU thickness (cm)	Percentage of THU (%)	TB/TT ratio
Non-sapropelic Marine	174 (112)	5.747	0.61	0.77	7 (3.9)	30	0.8
Upper Sapropel	114(62)	8.621	0.68	1.29	6.1 (3.6)	38	0.7
Lower Sapropel	287 (254)	3.484	1.12	1.68	15.7 (17.8)	35	0.6
Lacustrine	235(85)	4.255	0.8	1.9	20.8 (16)	53	0.3

Supplementary Table 1. Summary of THU list obtained from the core CS-14. Their depths, facies, thickness, mean ages are listed according to the stratigraphy. Average thicknesses and

average recurrence intervals of THUs for each facies, turbidite-homogenite ratios and the background sedimentation rates are listed at the rightmost columns.

Declaration of interests

The authors declare that they have no known competing financial interests or personal relationships that could have appeared to influence the work reported in this paper.

Highlights

- Multi-proxy parameters (XRF, AMS) are used to demarcation turbidite-homogenite units in the Kumburgaz Basin.
- 15 kyrs long sedimentary record of turbidite-homogenite units containing marine and lacustrine phases of Sea of Marmara.
- Turbidite-Homogenite intervals and thicknesses are affected by climatic changes, sea level and salinity of the region.

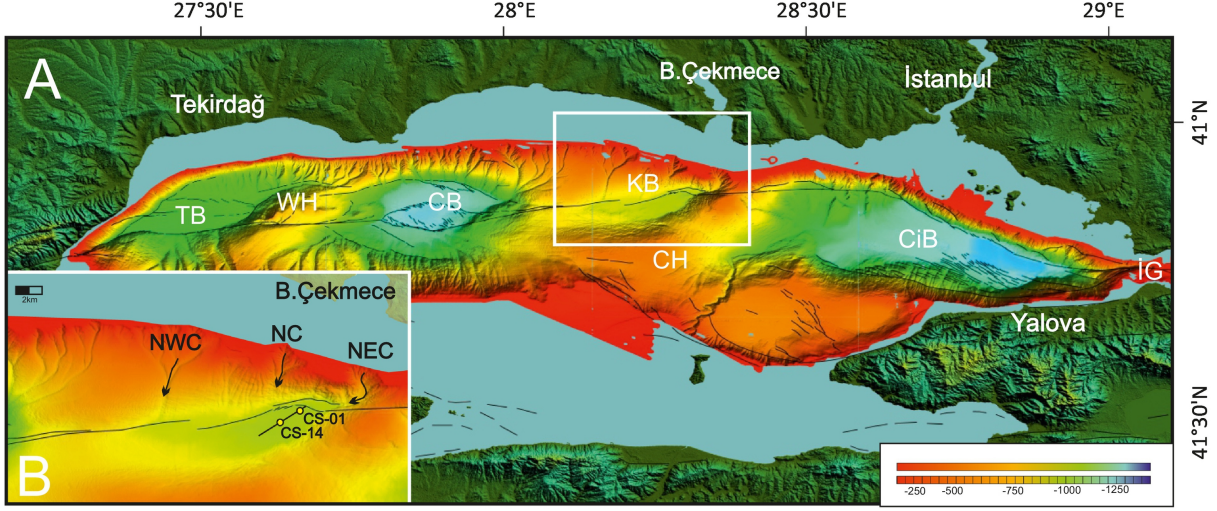
27°30'E
28°E
28°30'E
29°E
41°N
41°30'N
A
Tekirdağ
B.Çekmece
İstanbul
TB
WH
CB
KB
CH
CiB
İG
Yalova
2km
B.Çekmece
NWC
NC
NEC
CS-01
CS-14
B
-250
-500
-750
-1000
-1250

Figure 1

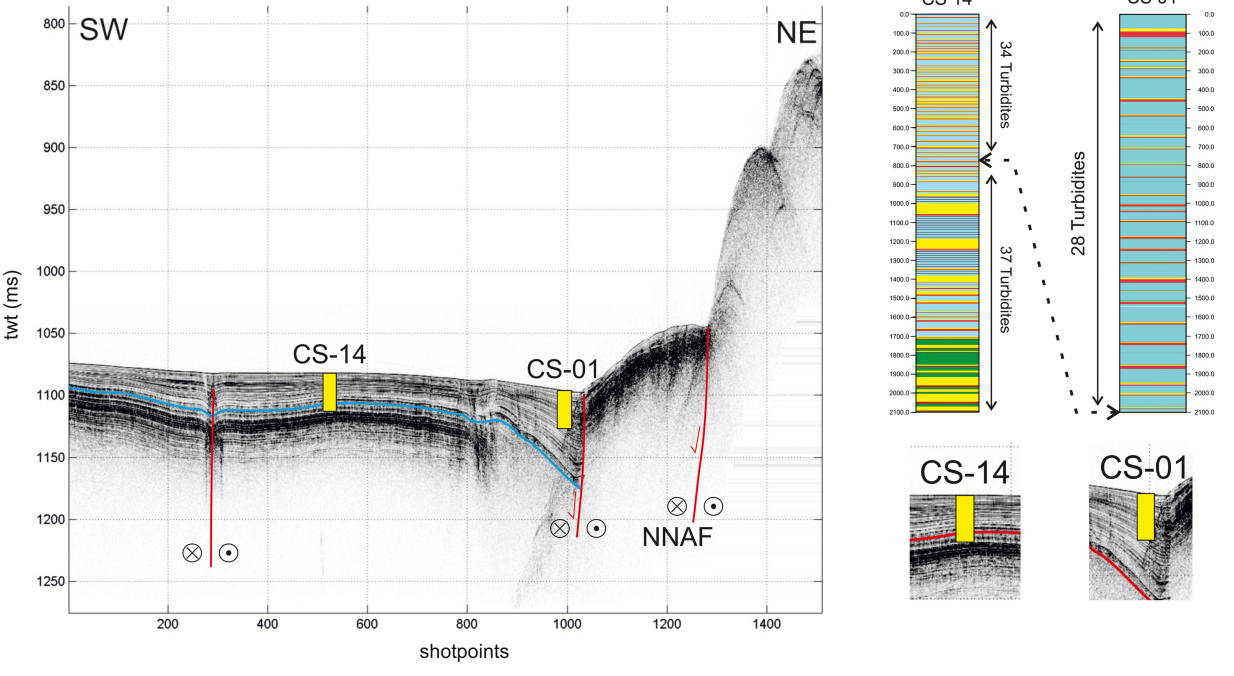
SW
NE
CS-14
CS-01
NNAF
twt (ms)
shotpoints
800
850
900
950
1000
1050
1100
1150
1200
1250
200
400
600
800
1000
1200
1400
CS 14
CS 01
34 Turbidites
37 Turbidites
28 Turbidites
CS-14
CS-01

Figure 2

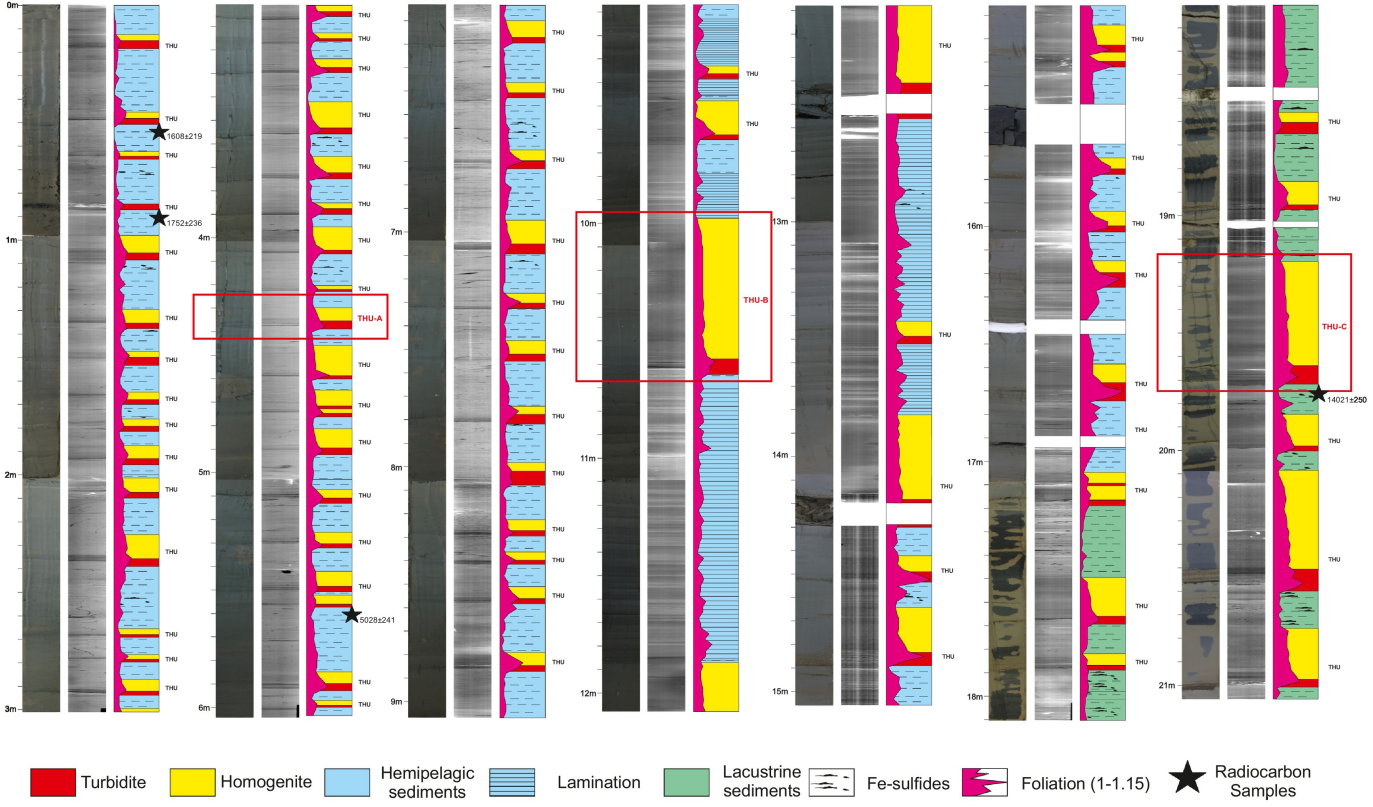
0m
1m
2m
3m
4m
5m
6m
7m
8m
9m
10m
11m
12m
13m
14m
15m
16m
17m
18m
19m
20m
21m
THU
THU-A
THU-B
THU-C
1608±219
1752±236
5028±241
14021±250
Turbidite
Homogenite
Hemipelagic sediments
Lamination
Lacustrine sediments
Fe-sulfides
Foliation (1-1.15)
Radiocarbon Samples

Figure 3

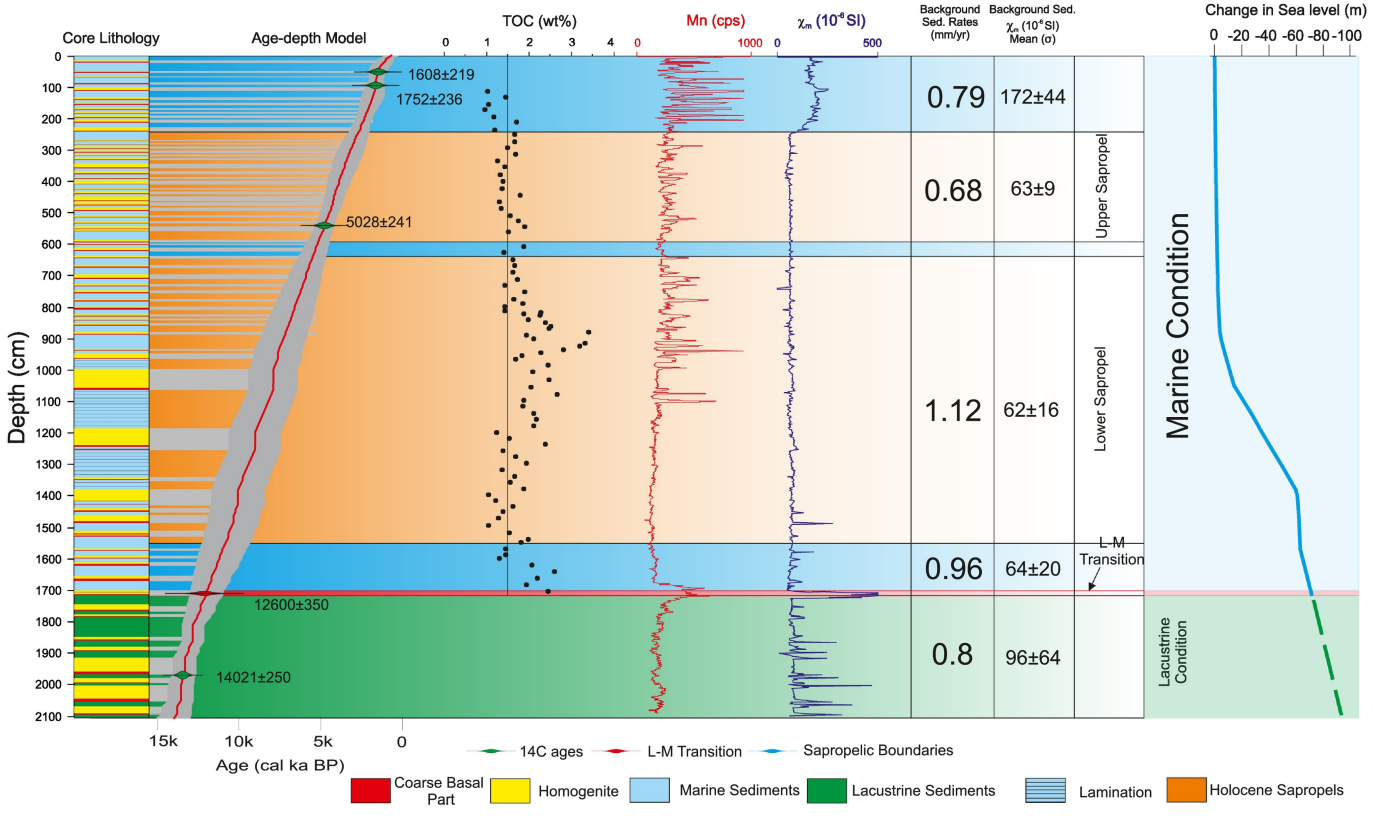
Core Lithology
Age-depth Model
TOC (wt%)
Mn (cps)
χ_m (10^{-6}SI)
Background Sed. Rates (mm/yr)
Background Sed. χ_m (10^{-6}SI) Mean (σ)
Change in Sea level (m)
0 -20 -40 -60 -80 -100
1608±219
1752±236
5028±241
12600±350
14021±250
0.79
172±44
0.68
63±9
1.12
62±16
0.96
64±20
0.8
96±64
Upper Sapropel
Lower Sapropel
L-M Transition
Lacustrine Condition
Marine Condition
Depth (cm)
Age (cal ka BP)
15k
10k
5k
0
14C ages
L-M Transition
Sapropelic Boundaries
Coarse Basal Part
Homogenite
Marine Sediments
Lacustrine Sediments
Lamination
Holocene Sapropels

Figure 4

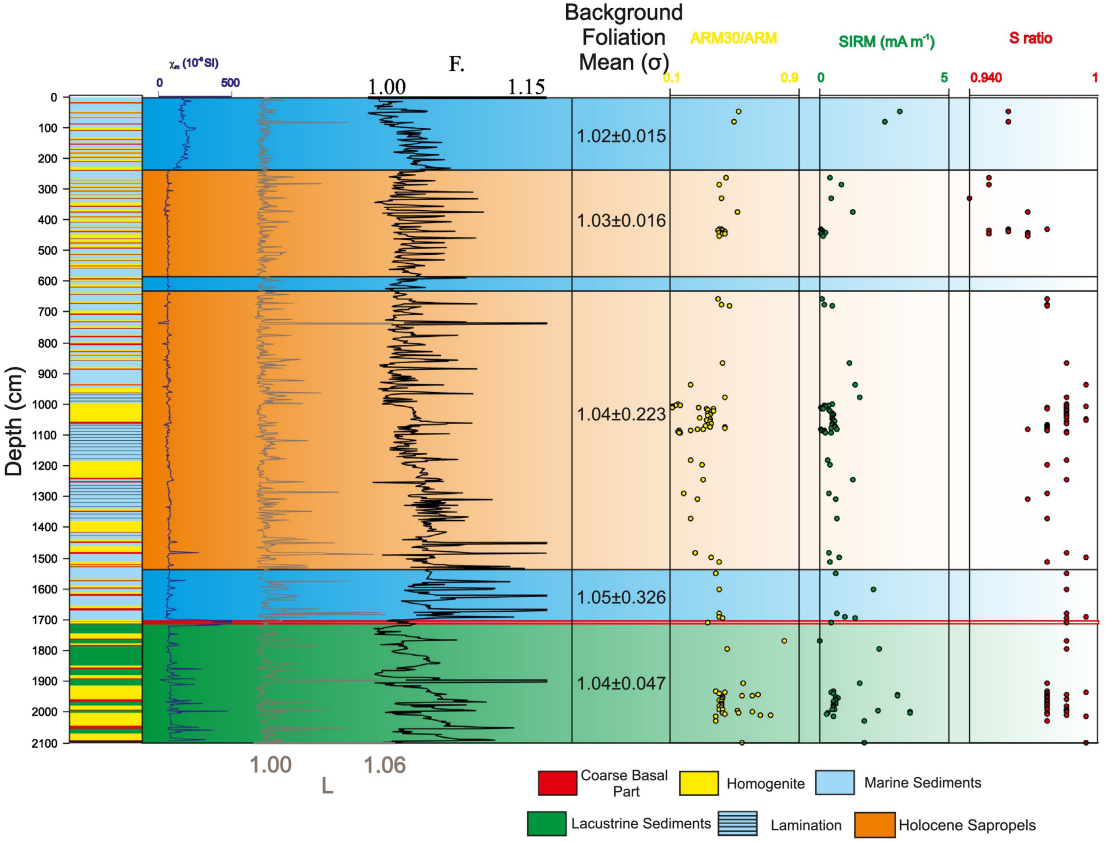
Background Foliation Mean (σ)
ARM30/ARM
SIRM (mA m-1)
S ratio
χlf (10-8 SI)
F.
L
Depth (cm)
1.02±0.015
1.03±0.016
1.04±0.223
1.05±0.326
1.04±0.047
Coarse Basal Part
Homogenite
Marine Sediments
Lacustrine Sediments
Lamination
Holocene Sapropels

Figure 5

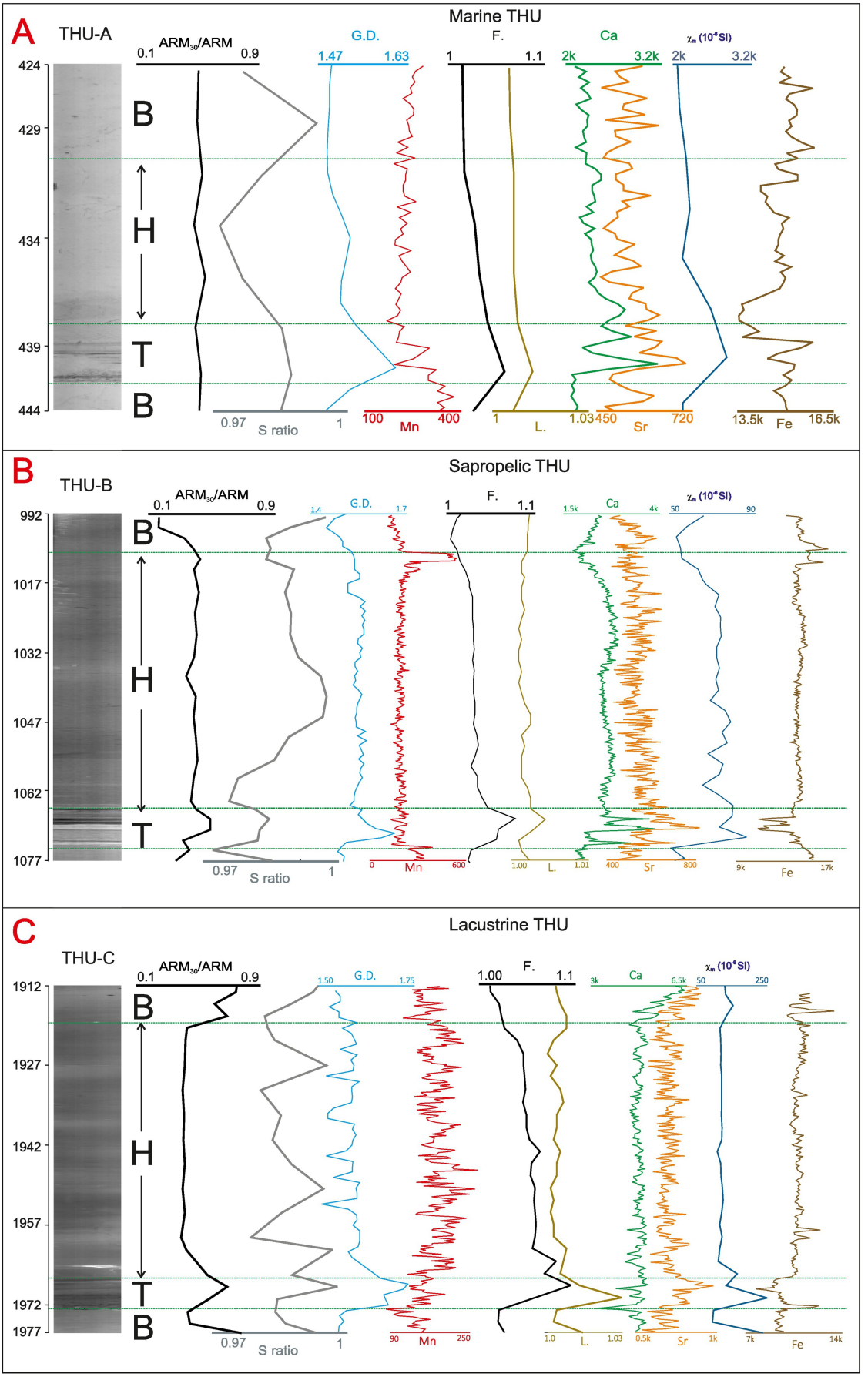
A
THU-A
Marine THU
ARM30/ARM
0.1
0.9
G.D.
1.47
1.63
F.
1
1.1
Ca
2k
3.2k
χm (10-8 SI)
2k
3.2k
424
429
434
439
444
B
H
T
B
0.97
S ratio
1
100
Mn
400
1
L.
1.03
450
Sr
720
13.5k
Fe
16.5k
B
THU-B
Sapropelic THU
ARM30/ARM
0.1
0.9
1.4
G.D.
1.7
1
F.
1.1
1.5k
Ca
4k
50
χm (10-8 SI)
90
992
1017
1032
1047
1062
1077
B
H
T
0.97
S ratio
1
0
Mn
600
1.00
L.
1.01
400
Sr
800
9k
Fe
17k
C
THU-C
Lacustrine THU
ARM30/ARM
0.1
0.9
1.50
G.D.
1.75
1.00
F.
1.1
3k
Ca
6.5k
50
χm (10-8 SI)
250
1912
1927
1942
1957
1972
1977
B
H
T
B
0.97
S ratio
1
90
Mn
250
1.0
L.
1.03
0.5k
Sr
1k
7k
Fe
14k

Figure 6

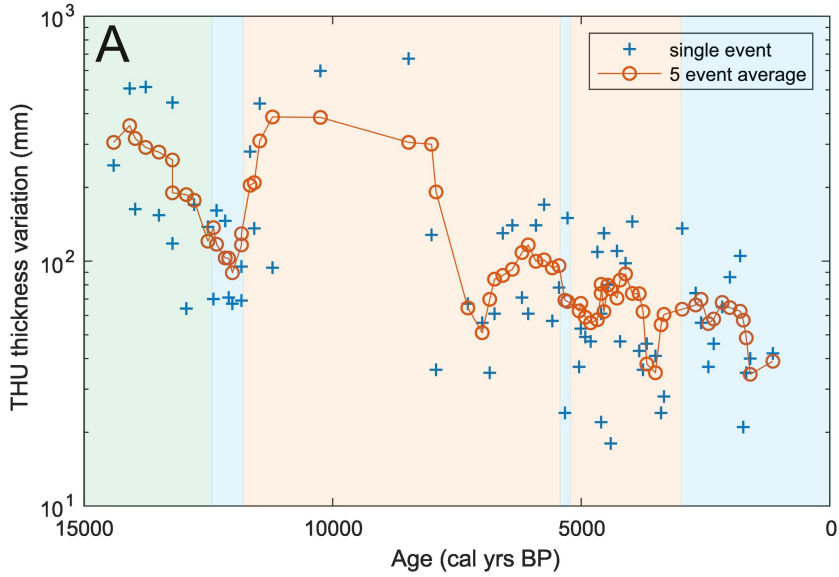
A
single event
5 event average
THU thickness variation (mm)
10^3
10^2
10^1
15000
10000
5000
0
Age (cal yrs BP)

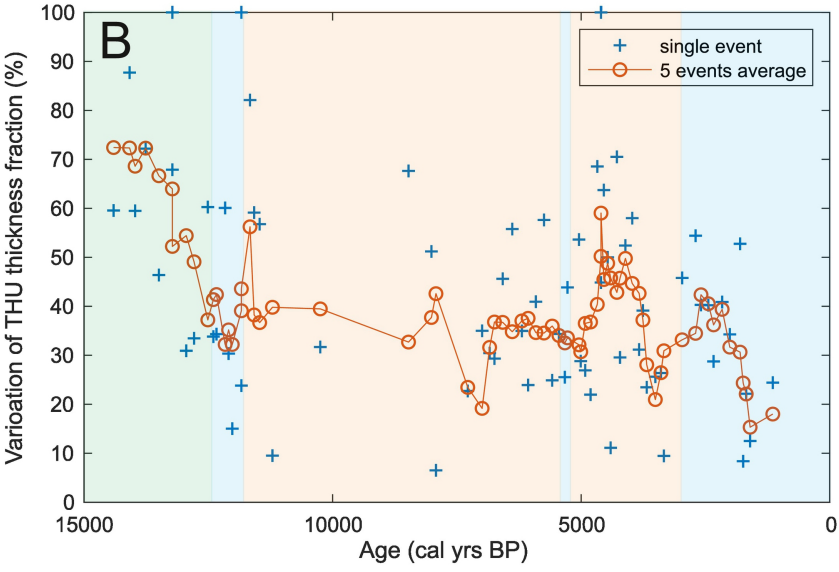
B
single event
5 events average
Varioation of THU thickness fraction (%)
100
90
80
70
60
50
40
30
20
10
0
15000
10000
5000
0
Age (cal yrs BP)

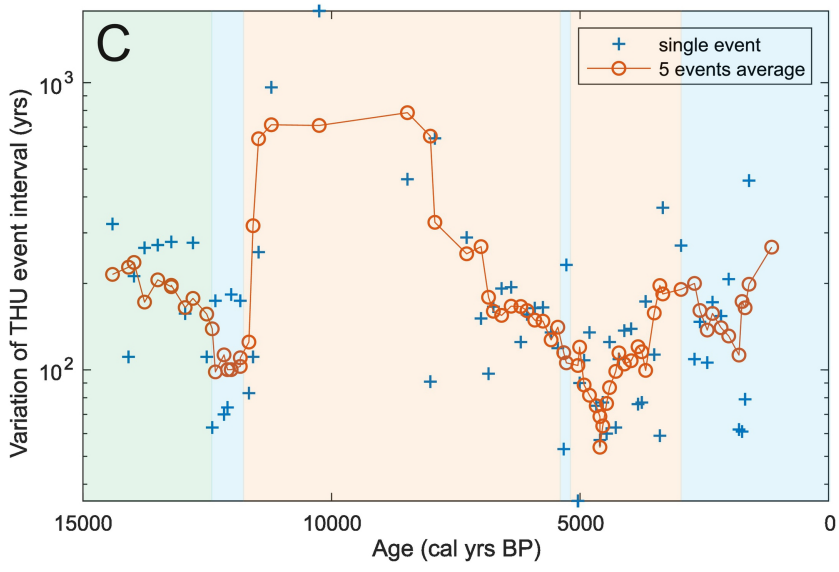
C
single event
5 events average
Variation of THU event interval (yrs)
10^3
10^2
15000
10000
5000
0
Age (cal yrs BP)

Figure 7